3 Inner Detector

3.1 Introduction

The ATLAS Inner Detector (ID) and its performance were described extensively in the ID TDR [3-1][3-2]. In this chapter, a summary of the results which are of most interest to physics analyses is given. In addition, updates arising from changes in the layout and further study are included. Despite various layout changes, the resolutions of the subdetectors and the number of hits on tracks have changed very little, hence the overall performance expected of the ID is very similar to that presented in the ID TDR.

The current baseline layout of the ID is described in Chapter 1. The ID consists of three subdetectors covering the range $|\eta| \leq 2.5$. The inner subdetector consists of three layers of pixel detectors, with a layer at a radius of 4 cm, called the *B*-layer, which is vital for good vertexing. Each pixel is 50 μm wide in $R\phi$ and 300 μm long. The SemiConductor Tracker (SCT) consists of four double layers of silicon strips. Each double layer consists of strips aligned in the azimuthal direction and strips rotated by a 40 mrad stereo angle with respect to the first set. The strips have an 80 μm pitch and are 12 cm long. The Pixel and SCT subdetectors are jointly referred to as the Precision Tracker. The outer subdetector, the Transition Radiation Tracker (TRT), consists of ~36 layers of 4 mm diameter straw tubes with resolutions ~200 μm, interspersed with a radiator to stimulate transition radiation (TR) from electrons. There are two thresholds for recording hits, the high threshold being used to detect TR photons.

In Chapter 1, the 98_2 layout, as described by the GEANT simulation and which was used extensively for the studies of this report, is shown. The differences between this layout and the current baseline layout are explained in a subsequent section.

Figure 3-i shows an example of the decay $B_d^0 \rightarrow J/\psi\ K_s^0$ in the Inner Detector.

3.1.1 Test-beam results

Pre-production modules are not yet available for the ID subdetectors. Nevertheless, there have been extensive tests of prototypes in test-beams. The hit resolution of the silicon detectors (pixels and strips) is well described by the pitch divided by $\sqrt{12}$: for the Pixels, see Chapter 8 of [3-3]; for the SCT see Chapter 3 of [3-1]. Because of the long pulse-lengths in the TRT, the readout of the TRT straws is sensitive to overlapping hits and consequently deteriorates at higher luminosities. A comparison between test-beam and the simulation for single straws as well as the luminosity dependence of the drift-time resolution can be found in Chapter 3 of [3-1].

Test-beam results for the TRT prototypes to study the transition radiation (TR) performance are discussed in more detail in Section 3.4.2.

3.1.2 Pattern recognition programs

Three pattern recognition programs (iPatRec, PixlRec and xKalman) have been used extensively to study the ID performance. These programs were described in some detail in Section 2.5.2 of the ID TDR and only a brief summary is given in this report. iPatRec searches for tracks using

space-points formed in the Pixels and SCT. Candidates are extrapolated to the TRT and drift-time hits added. This code is partially written in C++. PixlRec searches for tracks in the Pixels. Candidates are then extrapolated to the SCT. The Kalman Filter is used at the end of the pattern recognition phase to improve the track, add TRT hits and produce the final fit. xKalman searches for tracks in the TRT using fast histogramming of straw hits. Candidates are extrapolated to the SCT and Pixels to provide confirmation. The improved tracks are then extrapolated back into the TRT and drift-time hits added. Kalman Filtering techniques are used to extrapolate the tracks and remove wrong hits. At the time of writing, a new version of the code has been prepared in C++.

In addition, a program called ASTRA [3-4] has been used recently. ASTRA is an OO pattern recognition program designed and written in C++. It relies on iPatRec to provide space-points as input and returns track candidates which are fitted by iPatRec. The performance both in results and CPU-time consumption is very similar to that found by iPatRec.

The various programs have different advantages, for example xKalman is fast because it benefits from the histogramming in the TRT; iPatRec is less sensitive to interactions or bremsstrahlung. Nevertheless, the different programs have similar performance since they use the Precision Tracker to resolve ambiguities. In the future, effort will be made to consolidate the good features of the different programs.

3.1.3 Standard track quality cuts

Track quality cuts have been developed in the context of *b*-tagging (see Section 5.2 of the ID TDR). These cuts prove very useful in general, especially when it is important to ensure that a track comes from the primary vertex or a short-lived particle, such as a *b*-hadron. These cuts are particularly valuable in rejecting conversion electrons and they help to reduce the background to prompt muons from π/K decays. The basic track quality requirements are as follows.

- Number of precision hits ≥ 9 (out of a maximum of ~11, ignoring overlaps).
- Number of pixel hits ≥ 2 (out of a maximum of 3, ignoring overlaps).
- At least one associated hit in the *B*-layer.
- Transverse impact parameter < 1 mm.

Where it is important to ensure high track quality or the TRT transition radiation information is required, an additional cut on the TRT has been found to be useful. The extended track quality cuts have in addition.

- Number of TRT straw hits ≥ 20.

3.2 Detector layout

The detector layout was described in detail in the ID TDR [3-1][3-2]. There has been some evolution since then and summary of the design is given in Chapter 1.

3.2.1 Evolution since the ID TDR

A number of simulated layouts have been used for recent studies. These are:

ID TDR (96_12) This layout was used for the ID Performance TDR, Vol I. It did not completely correspond to the hardware description in Vol. II, because of time delays.

97_6 This layout corresponds to the hardware description in ID TDR, Vol. II [3-2].

98_2 This layout is identical to 97_6 for the ID description.

Pixel TDR This layout was updated from 97_6 to describe the layout in the Pixel TDR [3-3].

Material Report This layout was updated from Pixel TDR layout. It provides the best existing description of the ID material [3-5].

Current This is the current baseline layout, as described in Chapter 1.

The majority of studies undertaken for this report have used the 98_2 (97_6) layout. The principle differences of the various layouts are described below. For the studies described in this chapter, the differences in the layout are highlighted if the effects are significant.

Following the ID TDR layout, the 97_6 (equivalent to 98_2) layout was developed to include a change in the sign of the tilt angle of all pixel detectors to reduce cluster sizes, and an improved description of the ID services and the ID material. For the Pixel TDR, the layout was updated to include a new module design with thicker detectors, the change from four to five pixel disks in each end-cap, and small modifications to the barrel radii, number of ladders and detector tilt angles.

The design of the ID is now very close to being finalised. The 4th and 5*th* pixel disks have been moved to $|z| < 78$ cm to ensure that the Pixel system is contained within the ID barrel to avoid the beam pipe supports having to penetrate the Pixel end-caps. This only affects $|\eta| > 2.0$. Possible changes which are being evaluated include: extending the length of the pixel diodes to ensure that the electronics can be fitted into the design (see Section 3.2.1.2), fine-tuning of the SCT wheel positions to ensure hermeticity, and moving the non-emission getter (NEG) pumps into smaller $|z|$ (see Section 3.2.1.1).

3.2.1.1 TRT rates

The performance of the TRT depends critically on the hit rates in the straws. Figure 3-1 shows a comparison of the rates from the current best description of the ID material (corresponding to the so-called Material Report Layout) with the rates from the time of the ID TDR. Additional material in the ID volume increases the rate of secondaries, but this has been compensated by small reductions in the straw lengths. The net result is that the rates are little changed.

A further development which could affect the TRT rates is modifications to the beam pipe and the associated vacuum equipment. The non-emission getter (NEG) pumps consist of a thin layer of zirconium alloy sputtered on constantan strips placed on the inner surface of the beam pipe [3-7]. The main material components are the vacuum jacket and heaters. These pumps are designed to remove gas from inside the beam pipe. If they could be moved to smaller $|z|$, it may

be possible to avoid a bake-out of the beam pipe, which would necessitate the removal of the *B*-layer or the addition of unwanted insulation. Apart from significant mechanical considerations, this would have consequences for the backgrounds in the detector.

The beam pipe is modelled as 1 mm of beryllium. In one model, the NEG pumps can be represented as an additional 1 mm of beryllium at the radius of the beam pipe and with $|z| \geq 70$ cm. The increase in the TRT hit rate from secondaries at high luminosity is shown in Figure 3-2. The increases are 10-15% of the expected rates. Although not being catastrophic, increased hit rates will result in some degradation of performance.

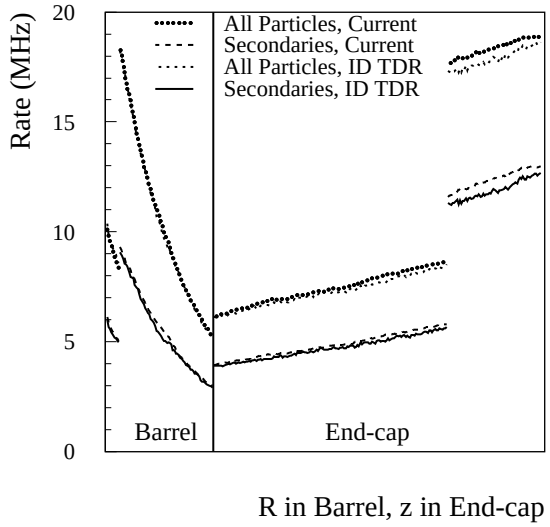

Figure 3-1 TRT hit rates at high luminosity. Comparison is made between the layout using the current best estimate of the material in the ID volume and the layout used for the ID TDR. The horizontal axis corresponds to layer number: in the barrel this corresponds to radius; in the end-cap this corresponds to *z*.

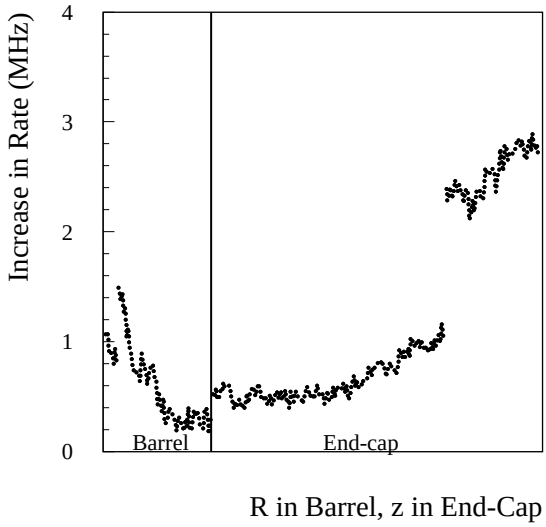

Figure 3-2 Increase in TRT hit rate arising from extended NEG pumps at high luminosity. The horizontal axis corresponds to layer number: in the barrel this corresponds to radius; in the end-cap this corresponds to *z*.

Changes to the beam pipe would also affect the impact parameter resolution. If the thickness of the pipe were doubled, then at $|\eta| = 0$, the multiple scattering term in the transverse impact parameter resolution would increase by 2.2%. A similar change would be expected if the radius of the beam pipe were increased from 25 mm to 35 mm.

3.2.1.2 Changes to the Pixels

It may prove necessary to increase the length of the pixel diodes. To study this in the simulation, the pixel dimensions were changed from $50\times300\ \mu m^2$ to $50\times400\ \mu m^2$. The changes in the transverse resolutions are fairly small, although not negligible due to charge sharing effects. Larger effects are seen in the longitudinal resolution, although the effects are less than might be expected, again due to charge sharing. Figures 3-3 and 3-4 show the comparison between the shorter pixels (used for all studies to date) and the longer pixels. While it may be necessary to lengthen the pixels, subsequent advances in technology may allow the detectors used for the *B*-layer to be constructed with $50\times300\ \mu m^2$ diodes at a later date. This would maintain the better impact parameter performance, since the resolutions are dominated by the design of the *B*-layer.

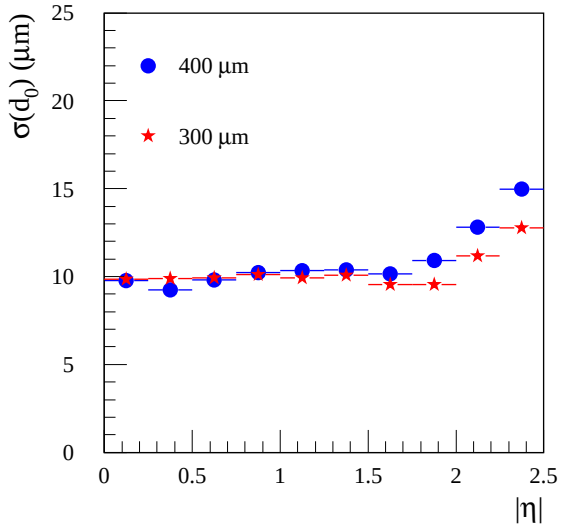

Figure 3-3 Transverse impact parameter resolution for high-p_T tracks. Comparison is made between 300 and 400 μm long pixels.

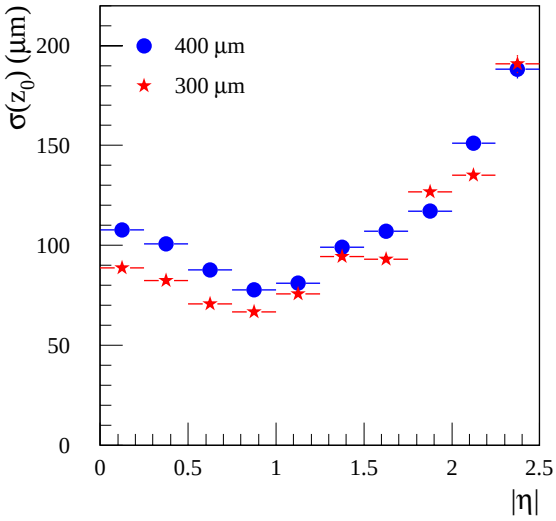

Figure 3-4 Longitudinal impact parameter resolution for high-p_T tracks. Comparison is made between 300 and 400 μm long pixels.

3.2.2 Material distributions

Since the ID TDR, there have been two studies of the material in the ID. The first was in Autumn 1997 where the possibility of reducing the number of precision layers [3-6] was considered. At that time, the description of the material was improved to bring the simulation in line with the engineering design presented in the ID TDR [3-2], resulting in layout 97_6 (equivalent to 98_2). The net increase in the Precision Tracker was small, but there was an increase of ~9% X_0 for $0.8 < |\eta| < 1.9$ in the TRT. The second study in Spring 1998 produced the Material Report Layout [3-5] where there was an increase ~5% X_0 for $|\eta| > 1.9$ in the Precision Tracker, with little net change in the TRT. Changes in the ID services outside the TRT have a relatively small effect on the performance of the ID and EM Calorimeter. The greatest sensitivity is to material within the volume of the silicon detectors, where the net increase from the ID TDR averaged over $|\eta| < 2.5$ is ~2% X_0 giving ~27% X_0; the corresponding numbers including the TRT are ~5% X_0 and ~48% X_0 respectively.

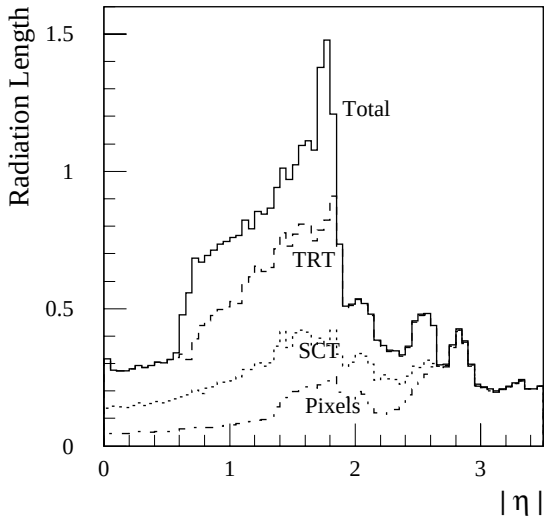

Figure 3-5 Material distribution of the ID vs |η| for the 98_2 layout, used in this report. The various bands include all services and supports within the corresponding fiducial volumes. The pixel band also includes the beam pipe. The total includes the ID services outside the TRT.

Figure 3-5 shows the material distribution for the ID corresponding to the 98_2 layout. This layout has been used for much of the simulation described in this report and provides a reasonable estimate of the material to be expected in the final design.

3.2.3 Magnetic field

The ATLAS solenoid [3-8] is 5.3 m long, compared with the 6.7 m length of the tracking volume of the Inner Detector. Consequently, the field deviates significantly from uniformity. Maps of the field are shown in Figures 3-6 and 3-7. The maximum value of the field depends on the current in the solenoid. The current proposed for the solenoid is that which would be required to produce a uniform 2 T field in an infinite solenoid in the absence of magnetic materials. With the same current, the maximum field in ATLAS will be about 2.09 T – this is enhanced by the iron in the Hadronic Calorimeter. It can be seen that B_z falls to about 1.0 T at the end of the solenoid and 0.5 T at the end of the detector. B_R becomes important for $|z| > 2$ m, with a maximum of ~0.8 T at the coil aperture.

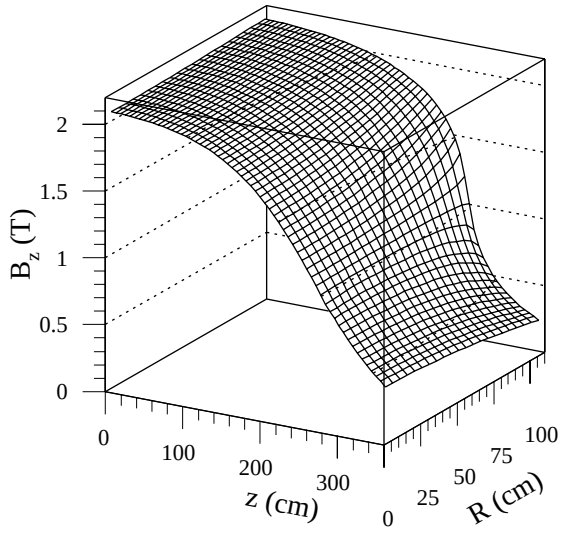

Figure 3-6 B_z as a function of z and R.

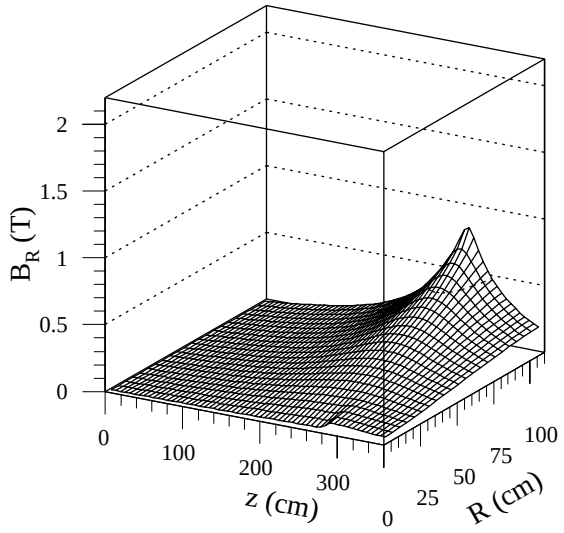

Figure 3-7 B_R as a function of z and R.

The consequences for the performance of the deviation of the field from uniformity are not major – the main effect is the need for more complex tracking algorithms which are consequently slower (this is a concern for the LVL2 trigger [3-9]). Most of the simulations discussed in this report has been performed with a uniform 2 T field. However, the track parameter resolutions presented in Section 3.3.1 explicitly show the effects of the solenoidal field, while the consequences for pattern recognition are examined in Section 3.5.4.

3.3 Reconstructed track parameters

The resolutions of the fitted track parameters are considered in this section. All results are shown for low luminosity. At high luminosity, there should be little effect on the hit resolutions of the silicon detectors. However, the spatial resolution of the TRT straws will be degraded (see Chapter 3 of [3-1]). The effects will be greatest at lower radii although these straws are less critical in the determination of the track parameters. Hence the net degradations expected at high luminosity are not great, as was shown in Chapter 4 of [3-1].

3.3.1 Muons

The track parameter resolutions have been estimated using the analytic calculations which were outlined in Chapter 4 of [3-1]. These calculations were shown to be in good agreement with a full simulation. Any small discrepancies between the full simulation and the analytic calculation are probably no bigger than the uncertainties of the real detector performance.

The calculations were updated to allow for an improved understanding of the material distributions and for the modifications to the Pixel layout. The net result of all changes relative to the ID TDR [3-1] is small. The largest changes are in the impact parameter resolutions caused by modifications to the Pixel layout. The transverse resolution at high p_T has improved slightly while the longitudinal resolution is slightly deteriorated. At low p_T, the resolutions are degraded by increases in the material in the Pixels. Detailed comparisons can be found in the Pixel TDR [3-3].

In the ID TDR, the parameter resolutions were shown for a uniform 2 T magnetic field. In the plots which follow, the baseline configuration is with the solenoidal field which will exist in ATLAS. For this simulation, the field was scaled to a maximum value of 2 T. Where appropriate, a transverse beam constraint has been included in the calculations.

3.3.1.1 Resolution in $1/p_T$

Figure 3-8 shows the resolution in $1/p_T$. The degradation in resolution caused by the solenoidal field compared to the uniform field is clearly visible for $|\eta| > 1.5$. The use of the beam constraint improves the resolutions by a few percent.

3.3.1.2 Resolution in ϕ

Figure 3-9 shows the resolution in ϕ. The degradation in resolution caused by the solenoidal field is only apparent at high p_T. The improvement obtained from the beam constraint is significant at lower p_T.

3.3.1.3 Resolution in cot θ

Figure 3-10 shows the resolution in cot θ. Measurements in the *R*-*z* plane are fairly insensitive to the distortions in the *B*-field and the use of a transverse beam constraint.

3.3.1.4 Resolution in d_0

Figure 3-11 shows the resolution in d_0. Since the determination of d_0 is dominated by measurements near the primary vertex, a region where the *B*-field is fairly uniform, there is a relatively small dependence on the field distortions. The performance seen at high p_T and high pseudorapidity is slightly different from that found in the full simulation (see Figure 3-3) because of the analytic calculation represents the *B*-layer $R\phi$ resolution as a constant, whereas in the full simulation, there is a small degradation associated with charge sharing.

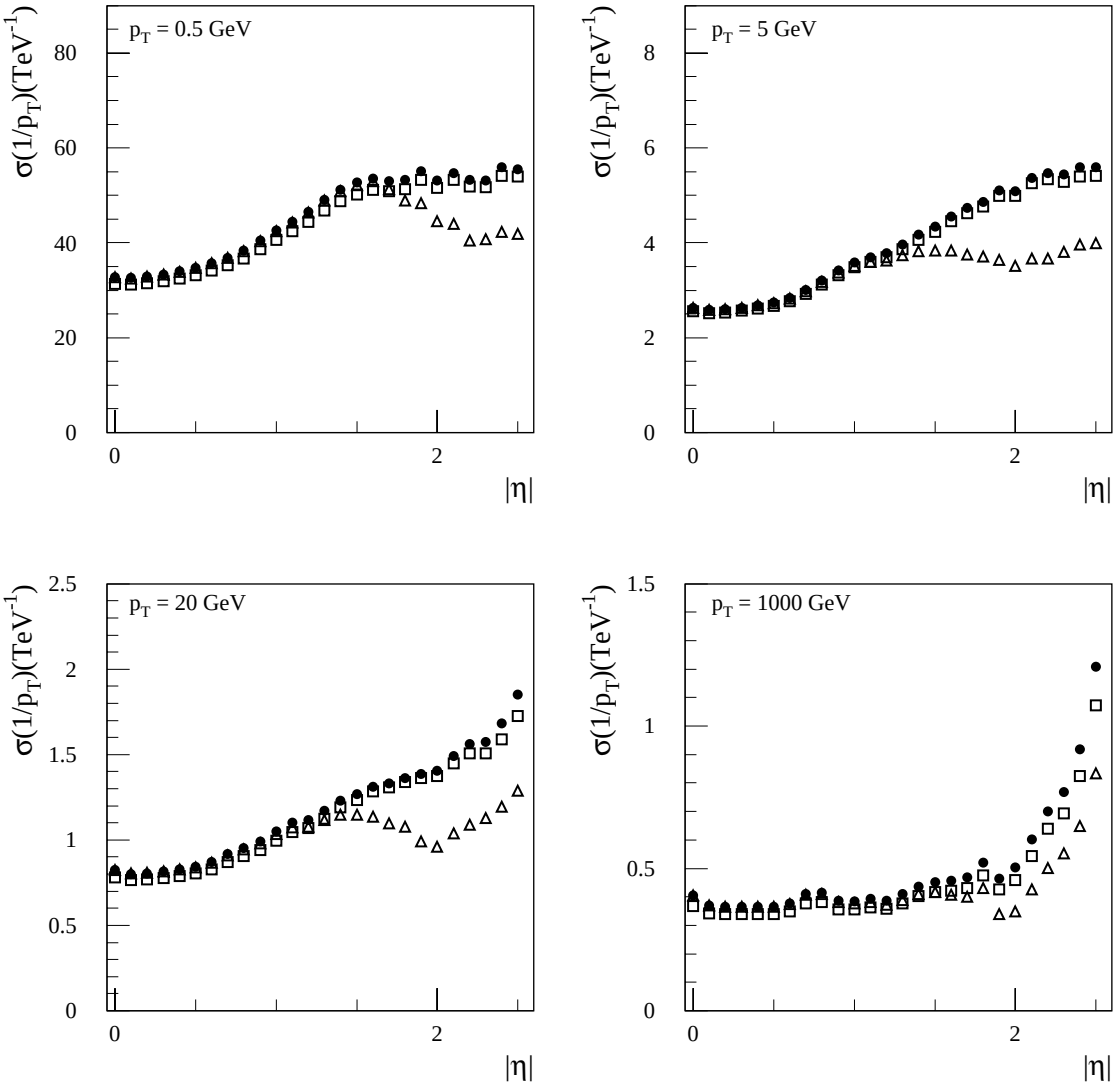

Figure 3-8 p_T resolution as a function of |η| for muons of various momenta. Results are shown for a solenoidal field without (circles) and with (squares) a beam constraint, and for a uniform field without a beam constraint (triangles).

3.3.1.5 Resolution in $\sin\theta \times z_0$

Figure 3-12 shows the resolution in z_0. What is generally of most interest is the projection of z_0 on to the plane transverse to the track direction – this is achieved by multiplying by sin θ. This corresponds to the measurement which is of most interest for vertexing and *b*-tagging and can be compared more directly with the transverse impact parameter d_0.

3.3.1.6 Simple parametrisations

If the features of the tracking system (the position and resolution of measurements, the location of material and the *B*-field) are uniform as a function of the transverse radius *R*, the resolutions can be expressed approximately in a simple form $A \oplus B/p_T$ [3-10]. This uniformity is achieved by design to a good approximation; however it deviates from this due to a reduced radial lever-

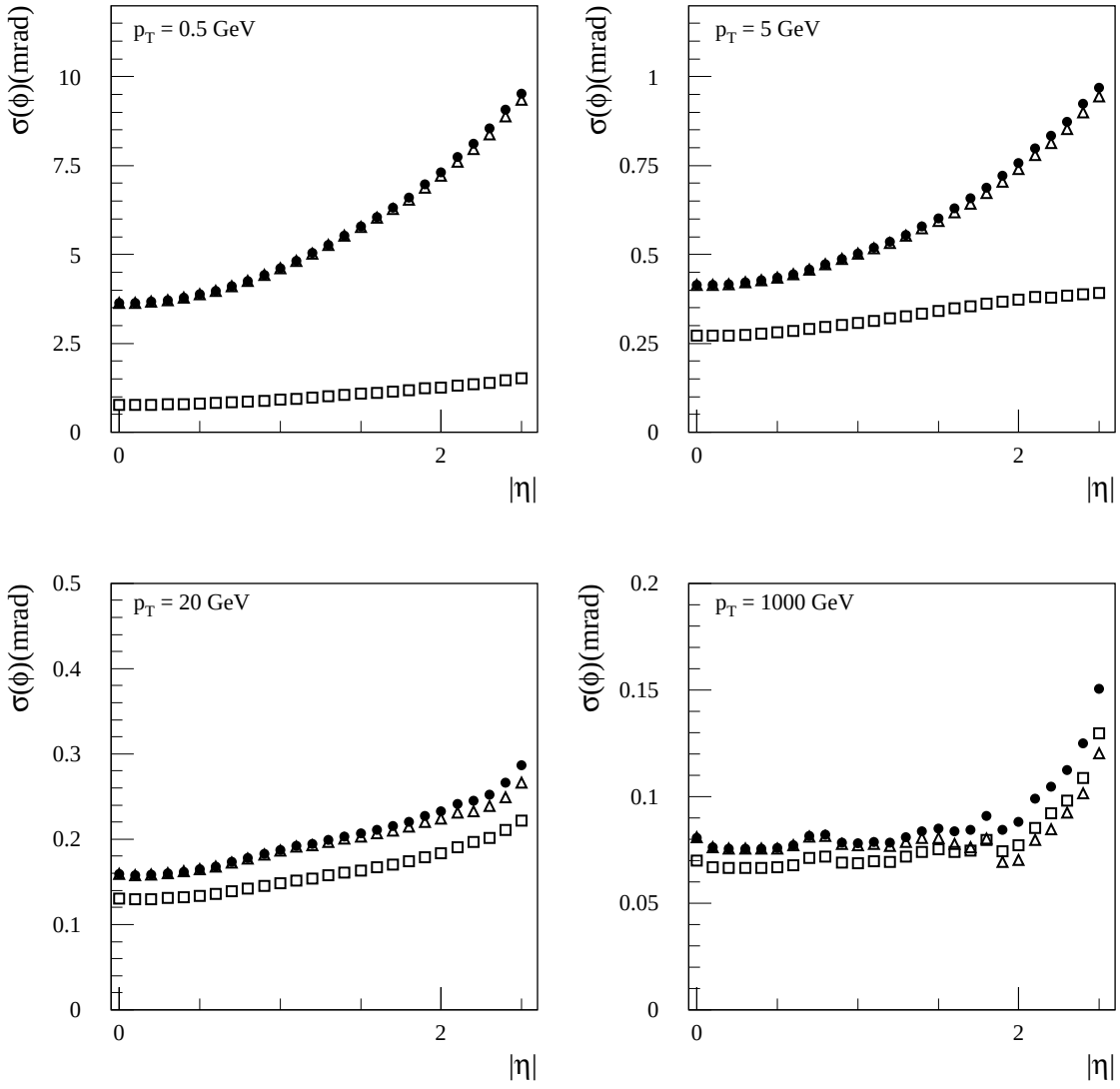

Figure 3-9 Azimuthal resolution as a function of |η| for muons of various momenta. Results are shown for a solenoidal field without (circles) and with (squares) a beam constraint, and for a uniform field without a beam constraint (triangles).

arm at high $|\eta|$, variations in detector spatial resolution as a function of $|\eta|$, a complex material distribution aimed at minimising material and including services, and a non-uniform field. Approximate forms for the resolutions as a function of p_T (in GeV) and θ for a solenoidal field without a beam constraint are:

$$\sigma\left(\frac{1}{p_T}\right) \approx 0.36 \oplus \frac{13}{p_T\sqrt{\sin\theta}} \quad (\mathrm{TeV}^{-1})$$

$$\sigma(\phi) \approx 0.075 \oplus \frac{1.8}{p_T\sqrt{\sin\theta}} \quad (\mathrm{mrad})$$

$$\sigma(\cot\theta) \approx 0.70 \times 10^{-3} \oplus \frac{2.0 \times 10^{-3}}{p_T\sqrt{\sin^3\theta}}$$

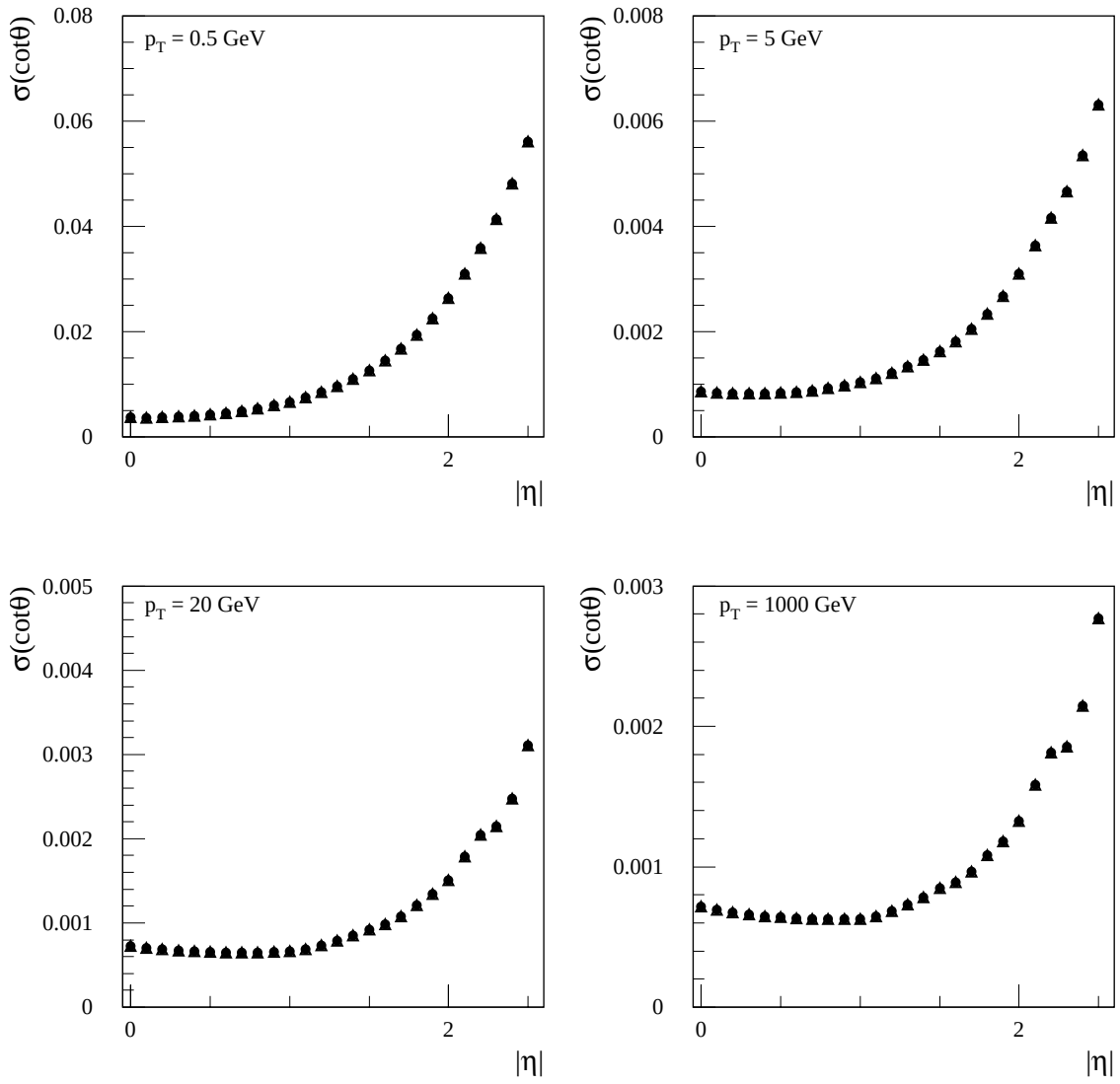

Figure 3-10 cot θ resolution as a function of |η| for muons of various momenta. Results are shown for a solenoidal field (circles) and for a uniform field (triangles) without a beam constraint.

$$\sigma(d_0) \approx 11 \oplus \frac{73}{p_T\sqrt{\sin\theta}} \quad (\mu m)$$

$$\sigma(z_0) \approx 87 \oplus \frac{115}{p_T\sqrt{\sin^3\theta}} \quad (\mu m)$$

The coefficients have been determined from tracks in the barrel with p_T = 1 and 1000 GeV.

Without the above approximations, the complete resolutions obtained for muons from the analytic calculation have been parametrised as a function of p_T and $|\eta|$ for various configurations [3-11][3-12] so that they can be used for fast simulation with the ATLFAST package (see Section 2.5). The p_T-dependence of the impact parameter resolutions is shown in Figures 3-13 and 3-14.

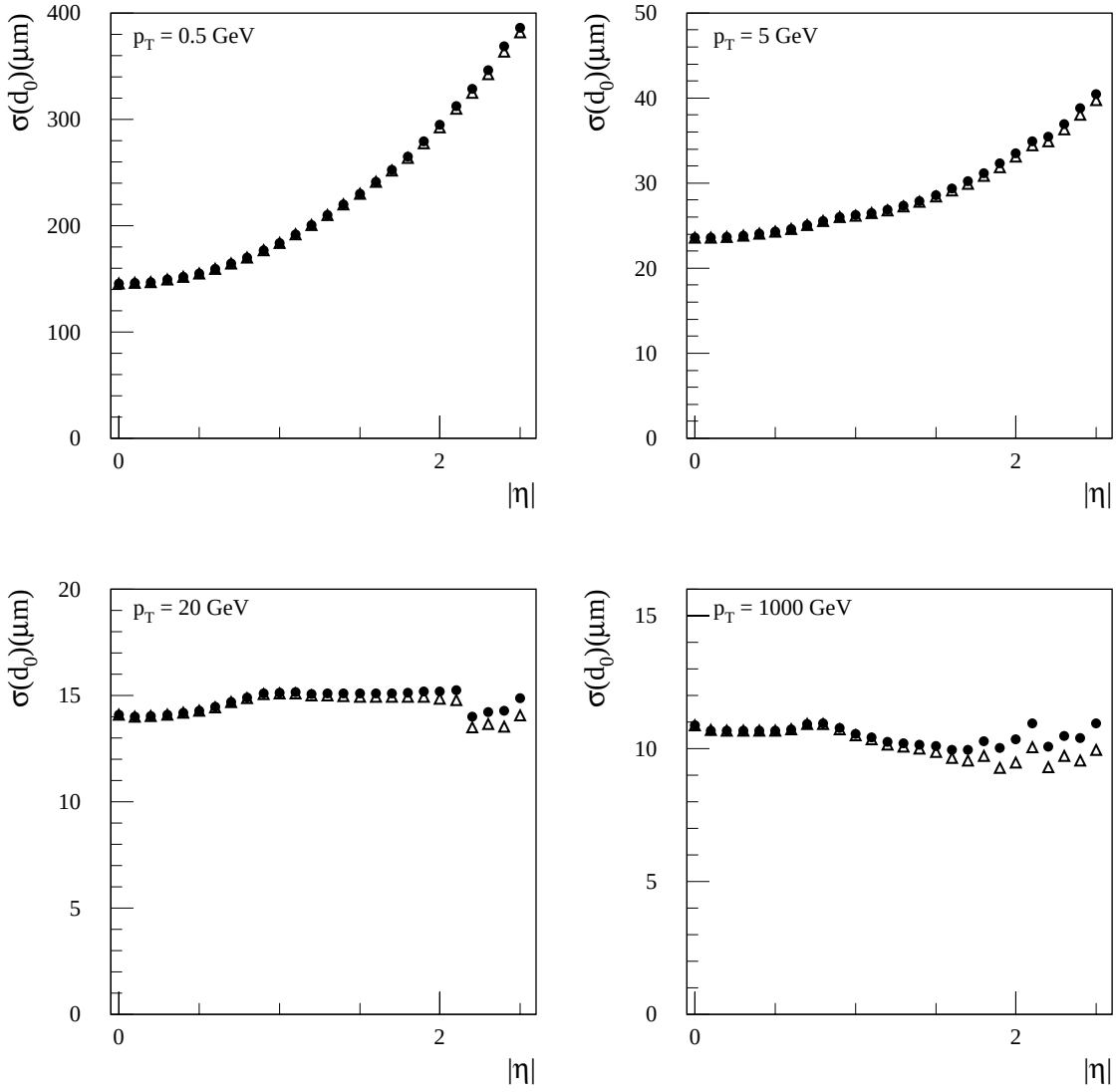

Figure 3-11 Transverse impact parameter (d_0) resolution as function of |η| for muons of various momenta. Results are shown for a solenoidal field (circles) and for a uniform field (triangles) without a beam constraint.

3.3.1.7 Correlations

The most important correlations occur between parameters in the transverse *x-y* plane ($1/p_T$, ϕ, d_0) and between those in the *R-z* plane ($\cot\theta$, z_0); however the two sets of measurements are largely decoupled. Figure 3-15 shows the normalised correlation coefficients for very low and very high p_T. At low p_T, the fitted angles and impact parameters are strongly correlated since they are dominated by the scattering in the material at the lowest radius (in particular in the *B*-layer).

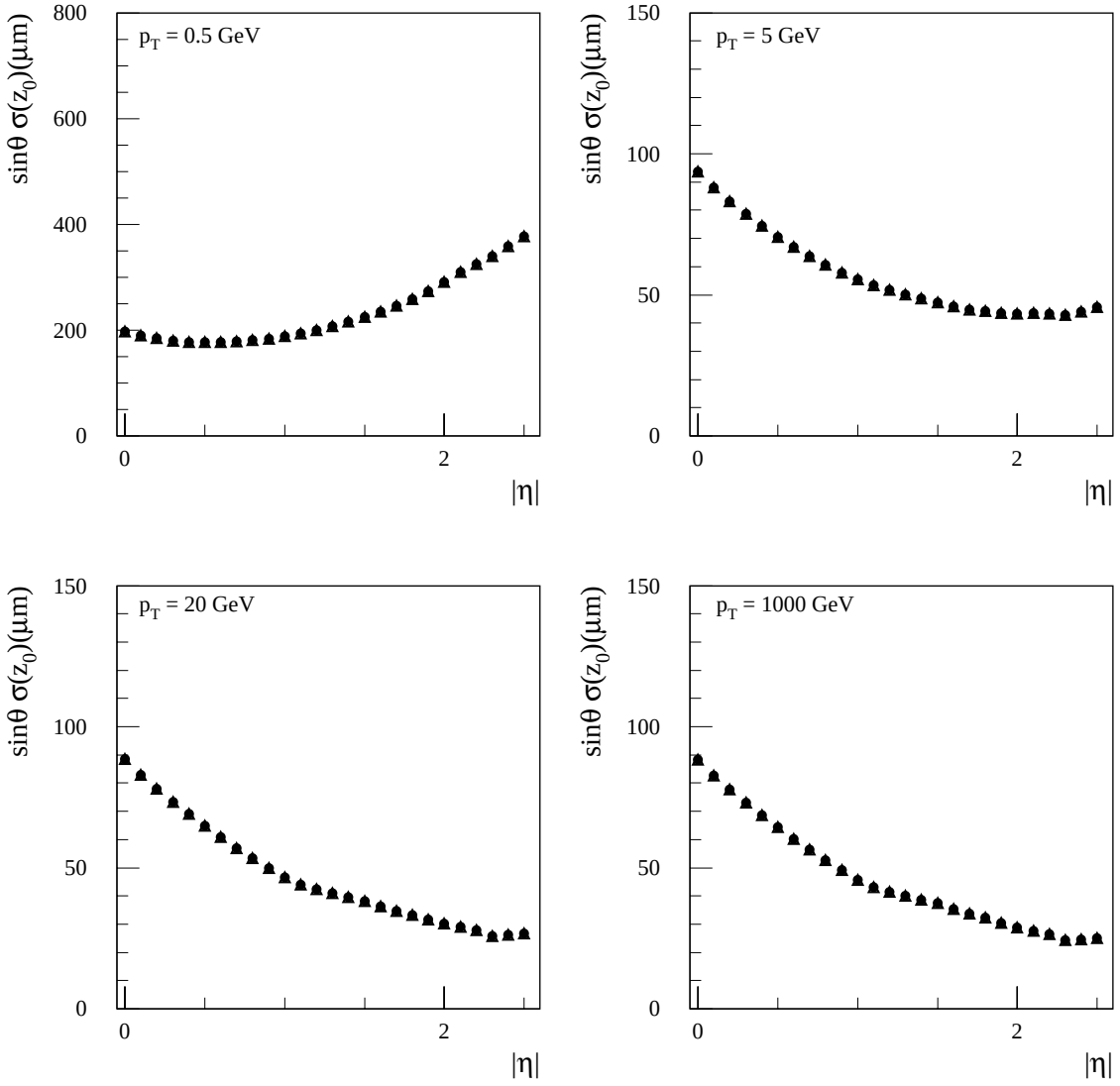

Figure 3-12 Longitudinal impact parameter (z_0) resolution projected transversely to the track direction as function of |η| for muons of various momenta. Results are shown for a solenoidal field (circles) and for a uniform field (triangles) without a beam constraint.

3.3.2 Other particles

The resolutions shown in the previous sections correspond to muons. These represent charged particles in the idealisation that there are no interactions other than multiple scattering. The distributions of reconstructed muon track parameters are very close to Gaussian, and in the absence of pattern recognition problems, do not have any significant tails (see Figures 3-19 and 3-20). In the ID TDR, it was shown that the fractions of tracks beyond 3σ in $1/p_T$ or d_0 are typically ~2% (see Section 5.1.2.1 of [3-1]). Small deviations from true Gaussian distributions arise from non-Gaussian components in the simulation of multiple scattering and from an incomplete description of the simulated material in the track fitting.

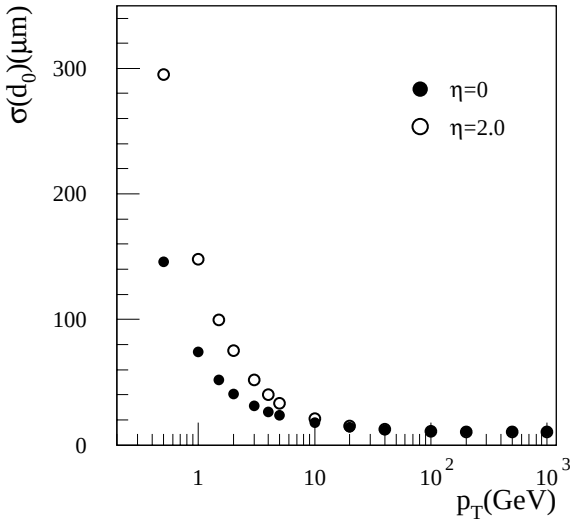

Figure 3-13 d_0 resolution as a function of p_T.

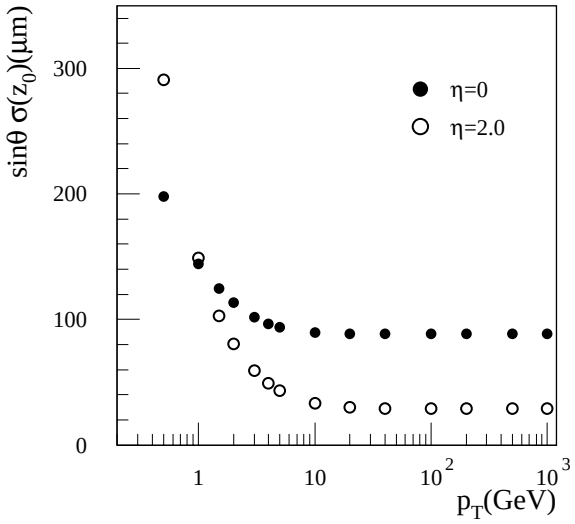

Figure 3-14 z_0 resolution as a function of p_T.

3.3.2.1 Pions

The probability for a pion to have a nuclear interaction is between 10 and 20% (see Chapter 3 of [3-1]). Interactions can cause tracks to be lost or produce tails in the reconstructed parameters. When track quality cuts (see Section 3.1.3) are applied, there is a reduction in track finding efficiency compared to muons (see Section 3.5.1.1) and the tails are greatly reduced. Consequently, the reconstructed pion track parameter distributions are very similar to those of muons (see Section 3.3.2.3).

For *B* physics studies using the fast simulation with the ATLFAST package, it is important to have a parametrised description of the pion track parameters for pions produced at or close to the primary vertex as well as for those which may be produced in the volume of the ID (arising from K_s^0 decays for example). Hence the distributions of track parameters for single pions and pions from K_s^0 decays were studied, using looser cuts to retain the decay pions. The track parameters were parametrised by the sum of two Gaussians as a function of p_T, $|\eta|$ and the production radius [3-12][3-13]. Nominally, the Gaussians describe separately the core and tail of the distributions, although, in practice, there is a significant correlation between the two and hence the interpretation of the parameters is not straightforward. Both Gaussians describe the five fitted track parameters and their correlations and the relative amplitude is determined by a fit to the impact parameter distributions. Further examples showing the comparison between full and fast simulation related to pions can be found in Section 17.2.2.2.

3.3.2.2 Electrons

An electron traversing the ID will emit bremsstrahlung as it crosses the material (see Figures 7-1 and 7-2 in Chapter 7). This introduces distortions to the track which cause the resolutions of the fitted parameters to be degraded and the reconstructed parameters to be biased. By using the so-called ‘bremsstrahlung recovery’ procedures (discussed in Section 7.2.1.1), it is possible to improve on average the reconstructed electron track parameters compared to the results which would be obtained using the same fitting procedure adopted for minimum ionising (non-radiating) particles. In what follows, electron track parameters have been obtained using bremsstrahlung recovery in the ID alone, as implemented in xKalman.

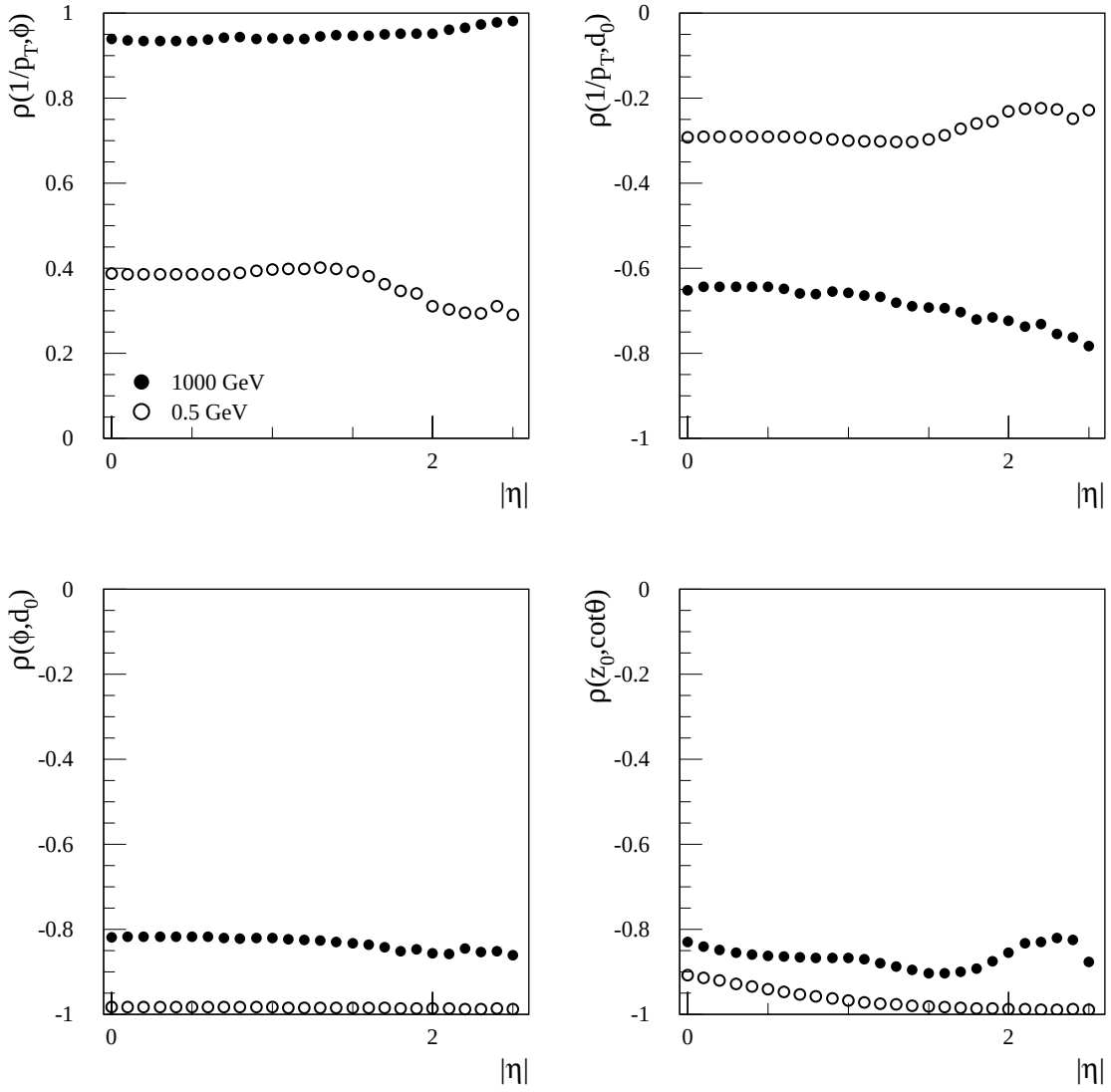

Figure 3-15 Correlations between track parameters for muons with p_T = 1000 GeV (filled circles) and 0.5 GeV (empty circles) in a solenoidal field without a beam constraint.

Figure 3-16 shows distributions for the reconstructed electron p_T. The distributions are significantly non-Gaussian (even for $1/p_T$) due to the bremsstrahlung which increases the track curvature causing the electrons to be reconstructed with a lower p_T. Since the radiation is almost collinear with the electron, it significantly affects all of the reconstructed track parameters in the bending plane ($1/p_T$, ϕ, d_0), but hardly affects those in the non-bending plane ($\cot\theta$, z_0). The correlation between the reconstructed transverse impact parameter and the reconstructed p_T is shown in Figure 3-17. The scatter plot exhibits structure (bands running top-left to bottom-right, at different angles) which corresponds to hard bremsstrahlung from different planes of material in the Precision Tracker.

Using distributions like those above for a variety of generated p_T's, parametrisations of the reconstructed electron track parameters were derived as a function of p_T and $|\eta|$ [3-12] so that they could be used for fast simulation with the ATLFAST package. For a given electron track, the parametrisation is derived from the location of a single hard bremsstrahlung chosen ran-

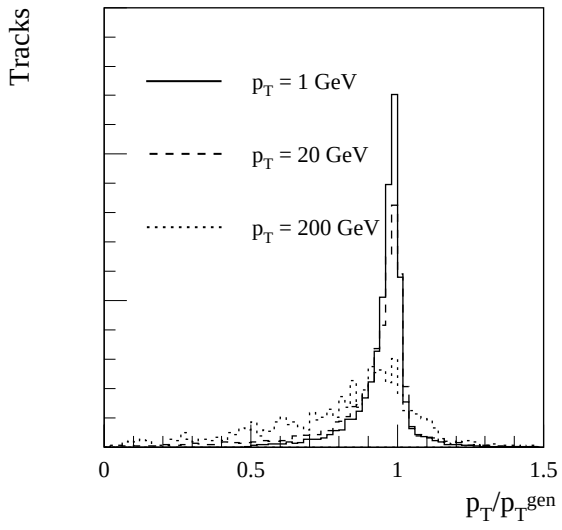

Figure 3-16 Ratio of reconstructed p_T to true p_T for electrons of various p_T's, averaged over |η|. The distributions are normalised to the same area.

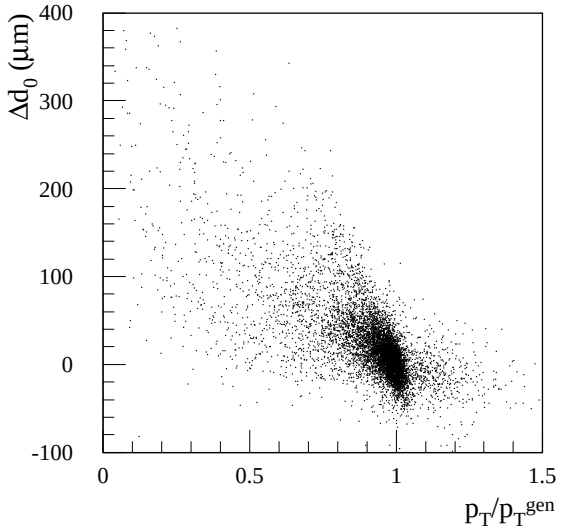

Figure 3-17 Difference between the reconstructed and true transverse impact parameter vs the ratio between the reconstructed and true p_T for 20 GeV electrons.

domly from the appropriate distribution. Plots showing the agreement between the full and fast simulation are shown in Figure 3-18. Further examples showing the comparison between full and fast simulation related to electrons can be found in Section 17.2.2.1.

3.3.2.3 Comparison between muons, pions and electrons

Figures 3-19 and 3-20 compare the reconstructed $1/p_T$ and d_0 distributions for muons, pions and electrons. The muon distributions are very Gaussian, the pion distributions have small tails while the electron distributions are significantly distorted. To compare the distributions, Gaussian fits were made to the cores of the distributions in exactly the same way for muons, pions and electrons. Since the electron distributions are significantly skewed, it was not simple to choose the range for the fit: for the $\Delta 1/p_T$ (Δd_0) distribution, the fit was made in the range ±1 (±2) times the rms centred on the peak. The fitted quantities were: the position of the peak, the rms and the tail fraction. The tail fraction was calculated as the fraction of the area of the distribution not contained in the Gaussian fit when extended over the complete range.

In Figure 3-21, these quantities are shown for 20 GeV p_T particles. The distributions for cot θ and z_0 are very similar for all particles. It can be seen that the peaks of the distributions are well centred for muons and pions, but there are significant biases for electrons. The resolutions for muons and pions are similar, but significantly worse for electron tracks. While the muons and pions have tails which are at the level of a few percent (these tails are sensitive to the fit range and are measures of the deviation from a perfect Gaussian; the actual number of muon 'outliers' is very small), the electron tails are very significant. Similar effects are seen at p_T = 1 GeV, although the electron tails are reduced by about a third.

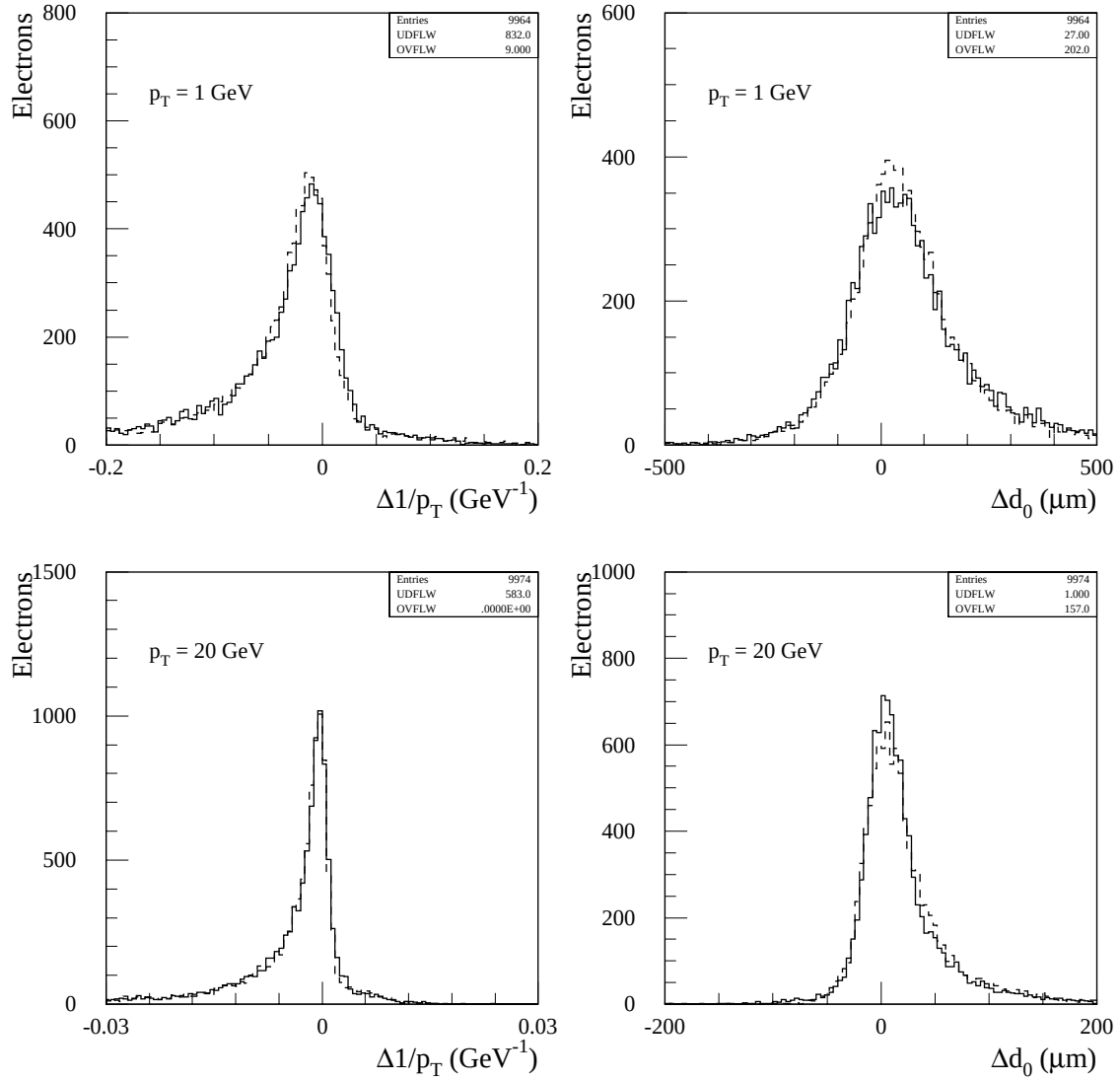

Figure 3-18 Differences between the reconstructed and true values of $1/p_T$ and transverse impact parameter for p_T = 1 and 20 GeV electrons. Comparison is made between fully simulated electrons (solid lines) and the fast simulation as used in ATLFAST (dashed lines). The fully simulated histograms are normalised to the same area as the fast simulation.

3.3.3 Charge determination

The specification on the p_T resolution (at high p_T) is set by the desire to be able to investigate the charge asymmetries in the decays of possible heavy gauge bosons *W*' and *Z*'. It is required that at p_T = 0.5 TeV, the sign of an electron should be determined to better than three standard deviations, corresponding to a misidentification probability of 0.13%. This means that the intrinsic resolution $\sigma(1/p_T)$ should be at least as good as 0.6 TeV^{-1}. From Figure 3-8 (p_T = 1000 GeV), it can be seen that this is satisfied for muons up to $|\eta| \sim 2.2$, beyond which the resolution degrades like $1/R^2$ due to the reduced lever-arm as tracks fail to cross the full radial extent of the ID.

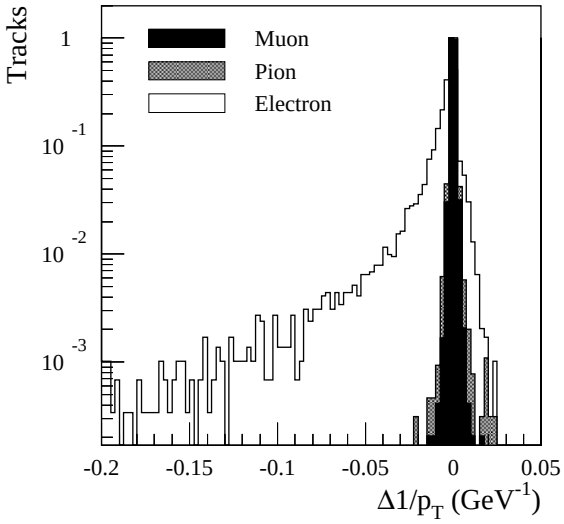

Figure 3-19 Difference between the reconstructed and generated $1/p_T$ for single 20 GeV negatively charged particles.

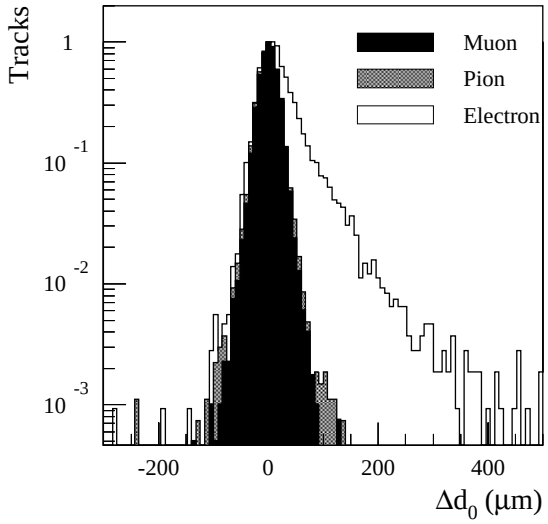

Figure 3-20 Difference between the reconstructed and generated transverse impact parameter for single 20 GeV negatively charged particles.

For electrons, the reconstruction of tracks is complicated by bremsstrahlung and subsequent conversions. In reducing the electron's momentum, the bremsstrahlung can also improve an electron's charge determination. Pile-up does not affect the charge measurement significantly. More details can be found in Section 4.2 of [3-1].

Using full simulation with additional smearing on $1/p_T$ to allow for the solenoidal field, the wrong sign fraction for electrons and muons (after a beam constrained fit) has been found as a function of p_T. The results, averaged over $|\eta| \leq 2.5$, are shown in Figure 3-22 and summarised in Table 3-1. The muons are well described by the intrinsic resolution; for electrons, this is only true at very high p_T. The effect of the *B*-field distortions is not great. Although the specification is not actually met for electrons, mainly because of tails arising from bremsstrahlung, the determination of the electron charge appears to be perfectly satisfactory up to ~1 TeV. The muon charge will be determined by the Muon System.

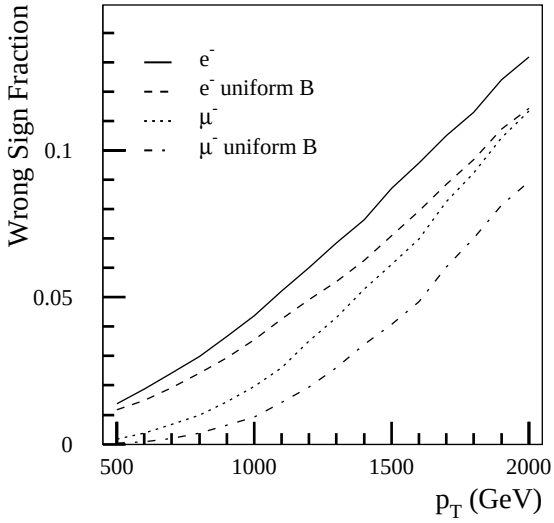

Figure 3-22 Wrong sign fraction as a function of p_T for muons and electrons, averaged over pseudorapidity in the presence of either a solenoidal or uniform magnetic field.

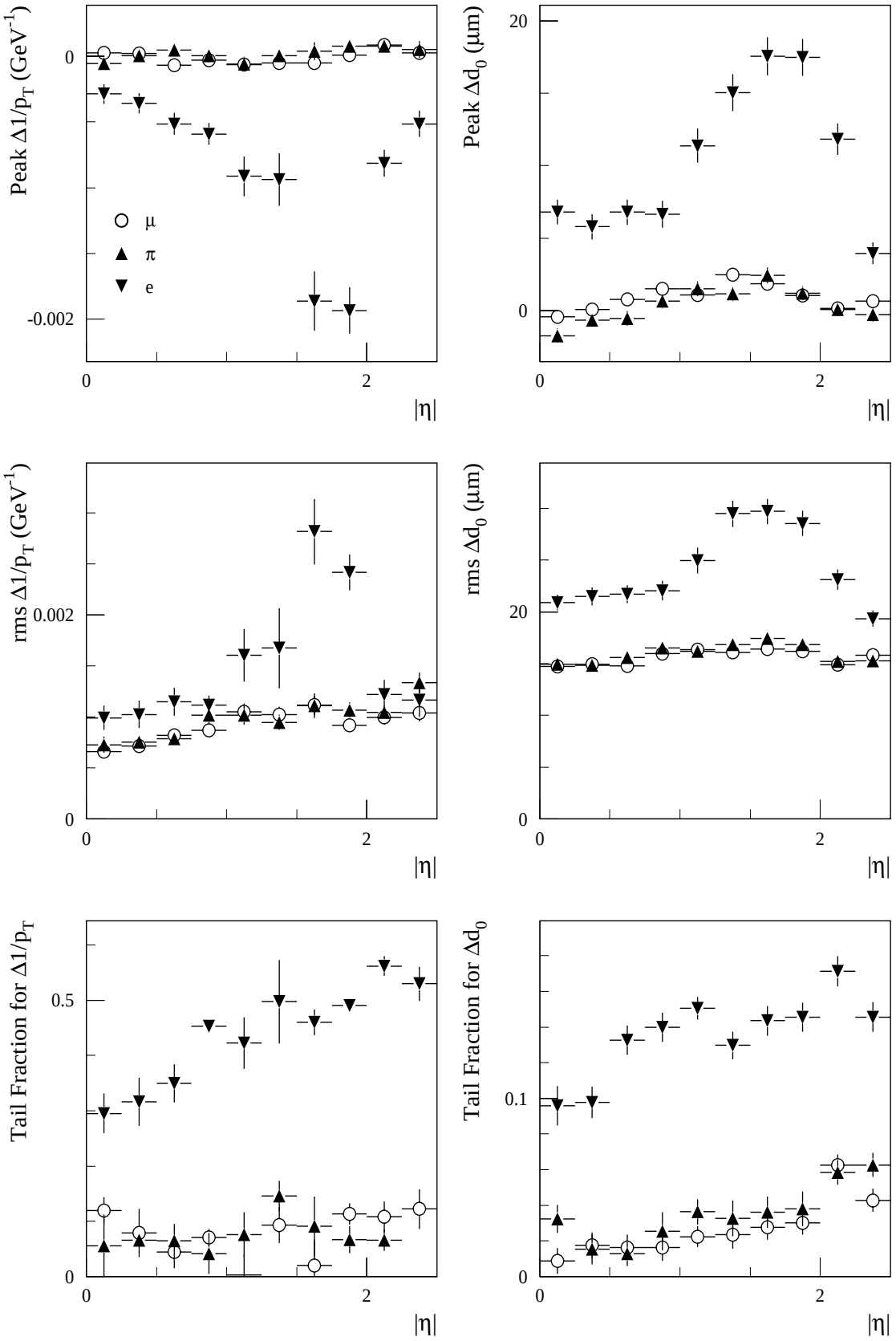

Figure 3-21 Comparison of fitted parameters for distributions of the reconstructed $1/p_T$ and d_0 for muons (circles), pions (up-triangles) and electrons (down-triangles) all with p_T = 20 GeV. See text for more details.

Table 3-1 Wrong sign fraction for high-p_T muons and electrons. Numbers in brackets are what would be expected from a Gaussian distribution with the nominal resolution.

p_T (GeV)	Wrong sign fraction (%)			
	Uniform *B* field		Solenoidal *B* field	
	Muons	Electrons	Muons	Electrons
500	0.04 (0.02)	1.2 (0.03)	0.2	1.4
1000	0.9 (0.9)	3.6 (1.2)	1.9	4.4
2000	9.2 (9.1)	11.5 (10.1)	11.6	13.3

3.4 Particle identification in the TRT

3.4.1 Use of transition radiation

The measurement of transition radiation (TR) in the TRT provides separation between hadrons and electrons. The emission of TR photons is a threshold effect which depends on the relativistic velocity p/m (and not p_T/m) and which turns on for $\beta\gamma > \sim 1000$ (see [3-14] for more details of the mechanism). Nevertheless, since p_T is the quantity of interest for many physics studies, the TR performance is examined as a function of p_T rather than p. The TR performance was discussed in Section 4.6 of the ID TDR [3-1]. In this section, a summary of the pion rejection is given.

Rejection against charged pions is achieved by counting the fraction of TRT straws which have a high-threshold (TR) hit. This has been studied for tracks which pass the extended ID track quality cuts described in Section 3.1.3, however, the results are not sensitive to the details of these cuts. Cuts on the fraction of TR hits as a function of p_T and pseudorapidity have been developed so as to maintain a specified electron efficiency for those electrons accepted by the quality cuts. The results shown in this section come from the description of the TRT used for the simulation at the time of the ID TDR and correspond to the physics studies presented in this report. Improvements in the understanding of the TR performance are discussed in Section 3.4.3.

Figures 3-23 and 3-24 show the pion efficiency for p_T = 2 GeV and 20 GeV, respectively, for 90% and 80% electron efficiencies. All the efficiencies are relative to the track quality cuts; to derive the total efficiencies, the numbers must be multiplied by the efficiencies to pass the quality cuts. The rejection, defined as the reciprocal of the efficiency, is best in the TRT end-cap where there is more TR radiator and a longer path length. Some of the variation with $|\eta|$ for fixed p_T arises from the fact that the TR rejection is more properly a function of p rather than p_T. For $|\eta| > 1.9$, particles leave the TRT through the last wheel and as pseudorapidity increases, the path length decreases causing a reduction in the pion rejection.

Figure 3-25 shows how the pion rejection varies as a function of p_T. As the electron p_T increases from 0.5 GeV, the electron radiation increases causing improved π/e separation. This is maximal for p_T around 2–5 GeV. At higher energies, the relativistic rise in dE/dx causes the pions to deposit more energy resulting in reduced separation. At high energies, $p > 100$ GeV, the pions emit TR photons at a comparable rate to electrons causing the separation to vanish. The plots shown so far correspond to single particles with no pile-up; the effect of pile-up can be seen in Figure 3-26. At high luminosity, other particles, including electrons from conversions, deposit energy in

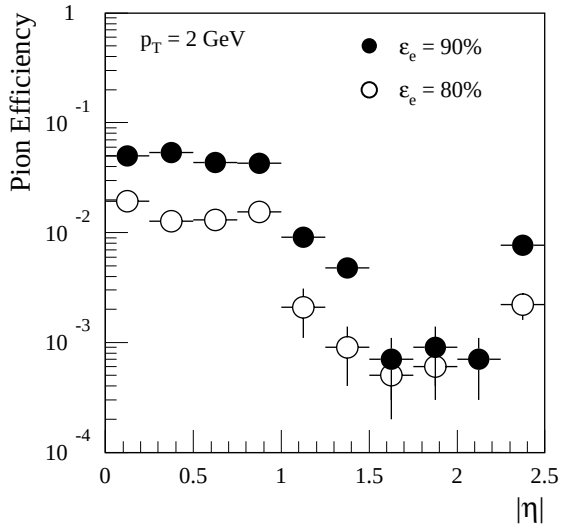

Figure 3-23 Pion efficiency as a function of |η| for p_T = 2 GeV for two different electron efficiencies. The efficiencies are relative; to get the total efficiency, the values must be multiplied by the efficiencies to pass the extended track quality cuts.

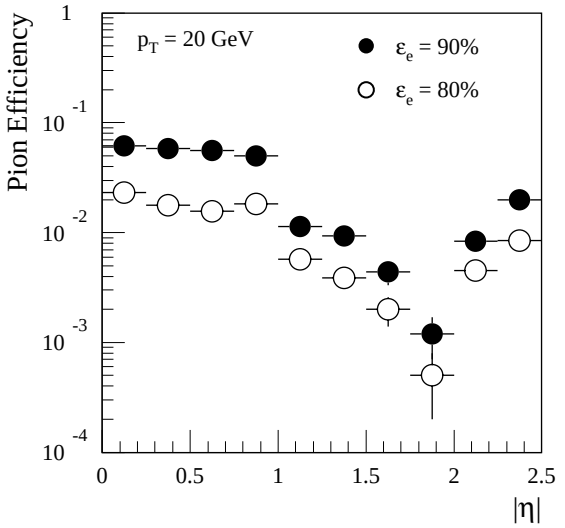

Figure 3-24 Pion efficiency as a function of |η| for p_T = 20 GeV for two different electron efficiencies.

the straws crossed by the particles of interest. This causes an increase in the number of high threshold hits for both pions and electrons, but the net effect is a degradation in the π/*e* separation.

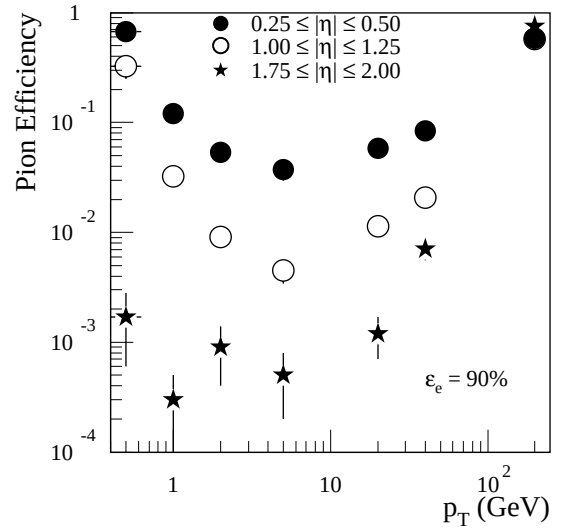

Figure 3-25 Pion efficiency as a function of p_T in various pseudorapidity intervals for 90% electron efficiency.

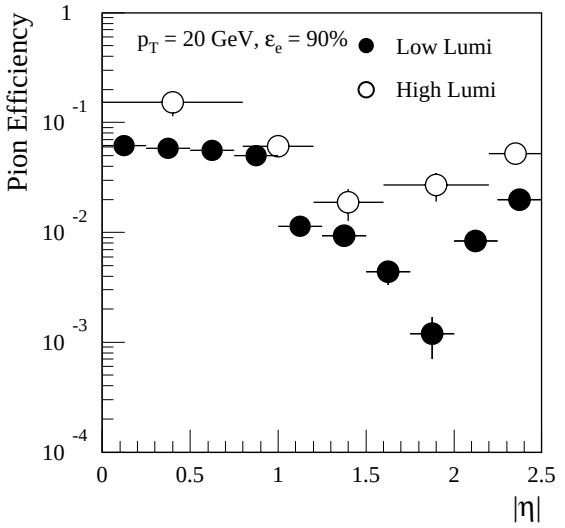

Figure 3-26 Pion efficiency as a function of |η| for low and high luminosity for p_T = 20 GeV for 90% electron efficiency.

3.4.2 Test-beam comparisons

The set-up used to make the test-beam measurements consisted of ten straws arranged one after another along the test-beam axis so that a single track could pass through all ten straws. There was a 2 cm gap between each straw into which samples of different radiator material could be placed. Each straw was read out by an ADC which was calibrated to the energy deposition in the straw. The set-up was studied with pions and electrons of 20 GeV in the H8 test-beam area.

Samples of 20 GeV pions and electrons were generated and tracked through a GEANT simulation of the test-beam apparatus. TR photons were generated and hits created by them were recorded during the tracking procedure. The response of each straw to the charged tracks and the TR photons impinging on it was calculated using a modified version of the TRT digitisation procedure. The simulation routines were tuned empirically to match the measured test-beam results. The comparison of data with Monte Carlo results is shown in Figures 3-27 (differential energy deposition spectrum) and 3-28 (the integrated probability that the energy deposition exceeds a certain threshold). The overflows, which are not visible in Figure 3-27, are 0.015 and 0.115 for the pions and electrons respectively, to be compared with the values of 0.015 and 0.123 respectively from the simulation. The rise in the differential distribution at very low energies is caused by the tracks which graze the straws very near the straw walls.

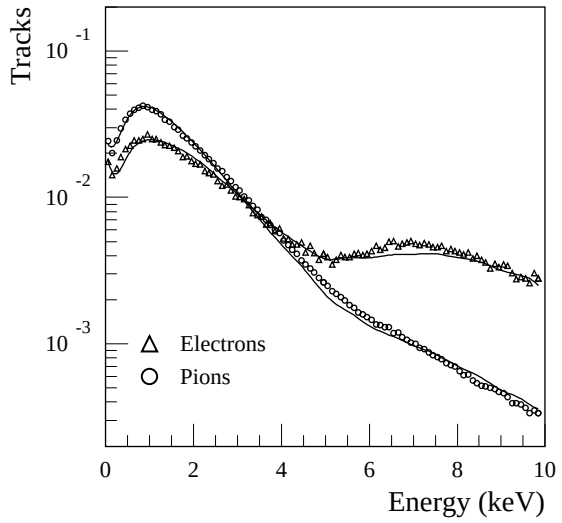

Figure 3-27 Energy deposition in TRT straws in the test-beam set-up for electrons and pions. The areas under the curves are normalised to unity. The associated lines come from the GEANT simulation.

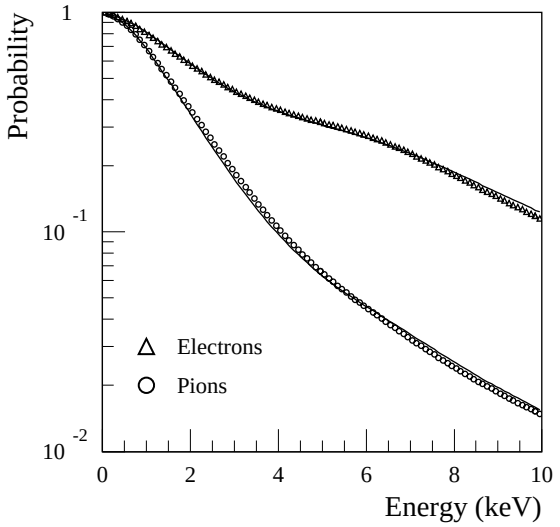

Figure 3-28 Probability that the energy deposition in TRT straws in the test-beam set-up exceeds the threshold (indicated by the horizontal axis) for electrons and pions. The associated lines come from the GEANT simulation.

3.4.3 Improved simulation

Figures 3-29 and 3-30 show the expected TR performance after improvements in the TR simulation, some of which are stimulated by the comparison of test-beam data with its simulation. Compared with the performance shown in Section 3.4.1, the expected performance for p_T = 2 GeV (Figure 3-29) has improved by a factor of ~2 in the barrel region and degraded by a factor of between 3 and 30 depending on pseudorapidity in the end-cap, although the best performance, which is achieved around $|\eta| = 1.7$, is little changed. At p_T = 20 GeV (Figure 3-30),

the performance has improved by a factor of ~2 in the barrel region and degraded by a factor of ~4 in the end-cap. The degradation in the end-cap is mostly due to the inclusion of the exact geometry foreseen for the radiator stacks, normalised to the recent test-beam measurements (in the ID TDR, the end-cap radiators were simulated as foam filling all the volume not occupied by straws). Also included in the improved simulation was a detailed description of the modular barrel TRT design including the carbon fibre module walls and inter-module gaps (in the ID TDR, the barrel geometry was simulated in a simplified way without explicit modules but with an equivalent amount of material) – this degrades the performance by ~20%. The other effects are linked to the better description of the *dE/dx* for pions and electrons as obtained from the recent test-beam measurements – this leads to a factor two improvement in rejection. A 5 keV simulated discriminator threshold was selected for identifying high threshold hits by systematically varying the threshold so as to obtain the optimal pion rejection. It was found that the rejection changes slowly as a function of this threshold.

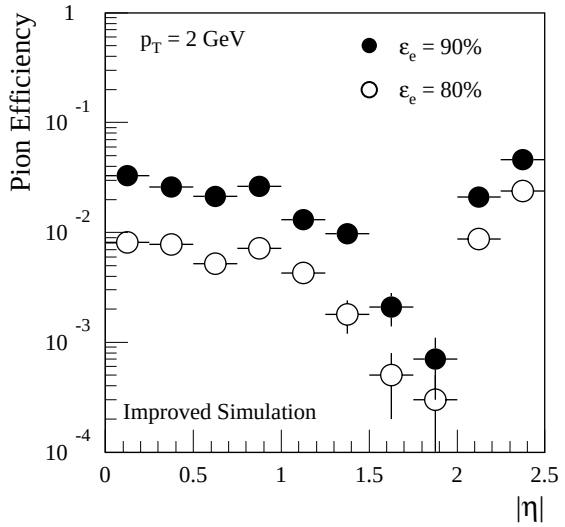

Figure 3-29 Pion efficiency as a function of |η| for p_T = 2 GeV for two different electron efficiencies using the improved TR simulation.

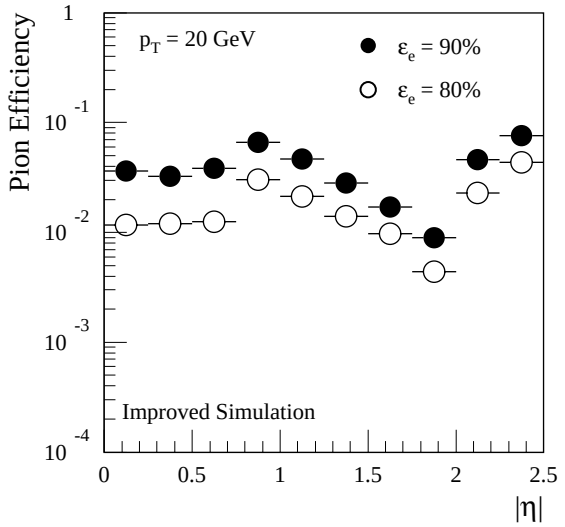

Figure 3-30 Pion efficiency as a function of |η| for p_T = 20 GeV for two different electron efficiencies using the improved TR simulation.

3.4.4 Particle identification by *dE/dx*

No charged hadron identification has been foreseen in the Inner Detector, because it is not necessary to fulfil the major physics goals of ATLAS. However, the absence of *K*-π separation is a clear handicap for some *B* physics studies such as the measurement of sin(2α), where the signal $B_d^0 \rightarrow \pi^+\pi^-$ channel is plagued by other two-body *B* decays involving kaons and protons (see Section 17.2.3). Even a modest (~1σ) *K*-π separation in the momentum range 4–50 GeV would help to separate statistically the signal contribution. Furthermore, the identification of highly ionising massive particles would be useful in the search for new particles in Gauge Mediated SUSY Breaking scenarios (see Section 20.3).

The design of the TRT allows for some *K*-π separation due to the significant relativistic rise of the ionisation loss (a factor of ~1.7) and to the high number of straws crossed, even though no pulse-height is measured. Three measurements can be used to estimate the specific ionisation:

the fraction of 'holes' (*i.e.* the absence of low-threshold hits) on a track, the fraction of high-threshold (TR) hits, and the measured drift-distance (both the shift and resolution of the drift-distance depend on the amount of charge deposited in a straw).

In this section, the results of a preliminary study [3-15] are presented. Figure 3-31 shows the probability to observe holes and high-threshold hits; Figure 3-32 shows the shift (and resolution) in the reconstructed drift-distance compared with the true value. Since the reconstruction of hits assumes that the corresponding particle travelled from the collision point at the speed of light, particles which travel more slowly will also give rise to reconstructed hits which are displaced. The ionisation in a given straw depends critically on the distance of closest approach of the particle to the wire and to the crossing angle with respect to the straw axis. Hence the measurements which are made must be parametrised in terms of these two variables in order to extract the specific ionisation.

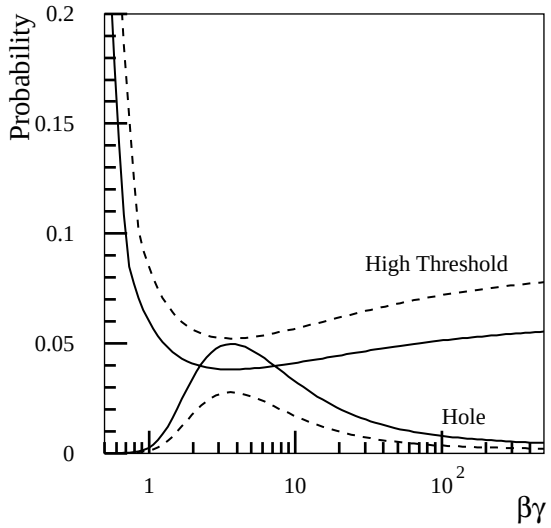

Figure 3-31 Hole and high-threshold hit probability as a function of βγ, for a straw (radius 2 mm) crossed at normal incidence at 1.5 mm (solid line) and 0.5 mm (dashed line) from the wire.

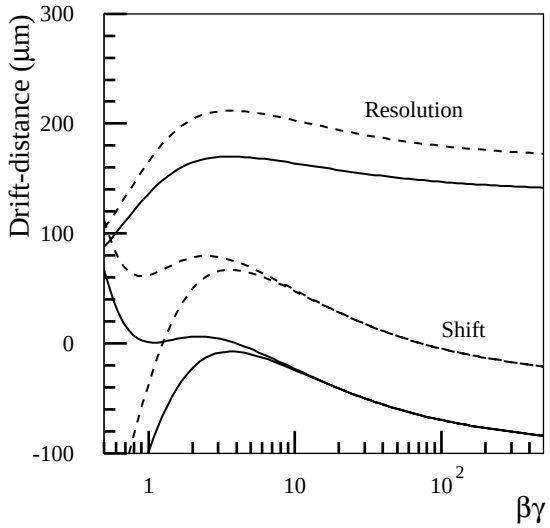

Figure 3-32 Drift-distance shift and resolution as a function of βγ, with the same conditions as in Figure 3-31. For the curves showing the 'shifts', the lower branches make no allowance for time-of-flight, while the upper branches allow for an average flight distance of 150 cm.

To obtain the shift of the measured drift-distance for each straw, the reconstructed drift-distance was compared to that estimated from the track fit where the hit on that straw was excluded from the fit. The resolution on the extrapolation is of the order of 100 μm (for a 5 GeV track), to be compared with the 180 μm drift-distance resolution. The track fit itself is not affected by the βγ dependence of the drift-distance as it is averaged with the left-right ambiguities. The track crossing angle and closest distance to the wire, the residual on the drift-distance, and the presence of a hole or high-threshold hit for each TRT straw were combined in an unbinned maximum likelihood fit for a given track (more details can be found in [3-15]). The fitted parameter is the logarithm of the 60% truncated-average energy deposit.

The performance of the algorithm was studied using full simulation for single particles with no pile-up, with the straw and electronic response tuned on test-beam data. The resolution for the logarithm of the energy deposit was found to be Gaussian (Figure 3-33) and independent of the momentum. The *p*-*K*-π separation depends of the position on the Bethe-Bloch curve (Figure 3-

34) and is best around a momentum (p not p_T) of ~5 GeV. At this momentum, the K-π separation is 0.9σ, while the p-π separation is 1.4σ and the p-K separation 0.5σ. The K-π separation drops to 0.5σ at 30 GeV momentum – this corresponds to a p_T = 5 GeV particle at $|\eta| = 2.5$. If the drift-distance information alone were used, the separation power would drop by only 10%, indicating that it is the most important single discriminant. Verification of this approach with test-beam data remains to be done, as does the study of the identification of massive slowly-moving particles.

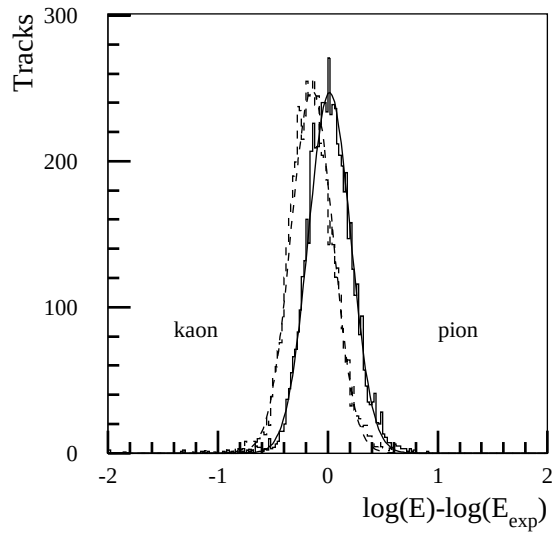

Figure 3-33 Comparison between energy actually deposited by a charged particle and the expected energy corresponding to a pion mass hypothesis, for p_T = 5 GeV pions (dashed line) and kaons (solid line).

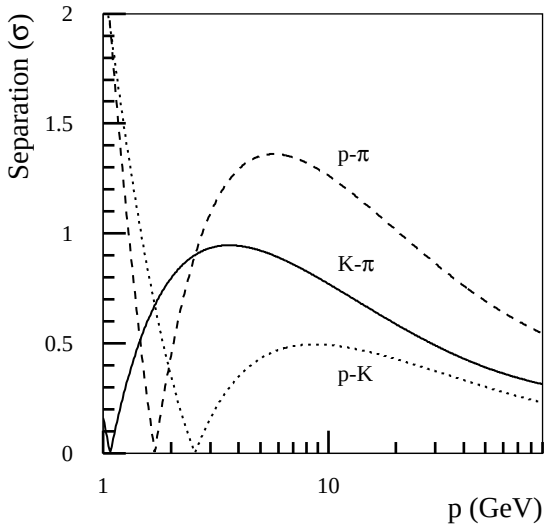

Figure 3-34 K-π, p-π and p-K separation as a function of momentum.

3.5 Pattern recognition

The performance of the pattern recognition programs was extensively analysed in Chapter 5 of the ID TDR [3-1] and [3-6]. To a large extent it has been found that iPatRec and xKalman give similar performance, implying that what was being studied arises from the design of the detector, the interactions of particles with the detector and the topology of the events being considered. More recently, tests were made with ASTRA (see Section 3.1.2), which gives results which are strongly correlated with those of iPatRec.

3.5.1 Isolated tracks

3.5.1.1 Basic results

The reconstruction efficiency for muons is determined mainly by the quality cuts (see Section 3.1.3), while for pions and electrons, it depends strongly on the interactions which the particles have with the detector and the magnetic field. It is important to contrast the efficiencies for track finding with some measure of the number of bad tracks found. Fake tracks are defined as those where ≤50% of the hits come from a single particle or which are associated with a

particle to which another reconstructed track is already associated. Even at high luminosity, the rate at which the pattern recognition programs reconstruct fake tracks which pass the quality cuts is very low: typically three orders of magnitude less than the rate of pile-up tracks and this can be reduced further by cutting on the TRT information. In addition to fake tracks, spoilt tracks are defined as those tracks whose reconstructed parameters are distorted by the inclusion of incorrect hits. For isolated tracks, these effects are generally less than those arising from interactions or bremsstrahlung (see Section 3.3.2).

Figure 3-35 shows the track reconstruction efficiency at low luminosity for isolated muons, pions and electrons of various p_T's (the efficiencies, averaged over $|\eta|$, are summarised in Table 3-2). The first three plots are shown for the basic track quality cuts. The muons and pions are not strongly affected by the requirement of TRT hits for the extended track quality cuts; by contrast, the electrons are strongly affected due to the effects of bremsstrahlung – their efficiency after the TRT cut can be seen from the last plot. The efficiencies are derived from xKalman. Since iPatRec does not start from the TRT, it is less susceptible to interactions in the Precision Tracker, and tends to result in somewhat higher efficiencies. Nevertheless, after the application of a TRT cut, the two programs give comparable results. The results presented in Figure 3-35, should be taken as indicative, since only in the case of decays of massive objects to leptons would one expect to find well isolated tracks and further, the efficiencies depend strongly on the algorithms used and the cuts applied. The single particle efficiencies have been parametrised as a function of p_T and $|\eta|$ [3-12] so that they can be used for fast simulation with the ATLFAST package.

Table 3-2 Summary of reconstruction efficiencies (xKalman) corresponding to Figure 3-35, averaged over |η|.

p_T (GeV)	Reconstruction Efficiency (%)			
	Basic Cuts			Extended Cuts
	Muon	Pion	Electron	Electron
200	98.6	94.9	95.9	94.8
5	98.2	89.5	90.4	84.4
1	96.8	84.0	76.4	69.4

3.5.1.2 Effect of pile-up

It was shown in Chapter 5 of the ID TDR that the pattern recognition performance depends little on the presence of pile-up at high luminosity. Despite high occupancies at high luminosity (10–40%), the TRT continues to function well for pattern recognition even in stand-alone mode, due to the large number of straws (this is illustrated in Figure 12-2 of [3-2]).

3.5.1.3 Effect of detector noise

Figure 3-36 shows the fake rate at high luminosity and the reconstruction efficiency for single tracks as a function of the fraction of noisy strips in an SCT module. The fake rates are shown for relaxed cuts in order to have an observable number of fakes. If the cut on the number of precision hits is tightened from 7 to 9, then the fake rate falls by an order of magnitude. The rates are shown for $p_T > 5$ GeV; they are a factor of ~3 higher for $p_T > 2$ GeV. The fake rate rises dramatically with the fraction of noisy strips, and for ~1% noisy strips (albeit with the relaxed cuts of ≥7 precision hits)), approaches the rate of real pile-up tracks with $p_T > 2$ GeV (2×10^{-2} in

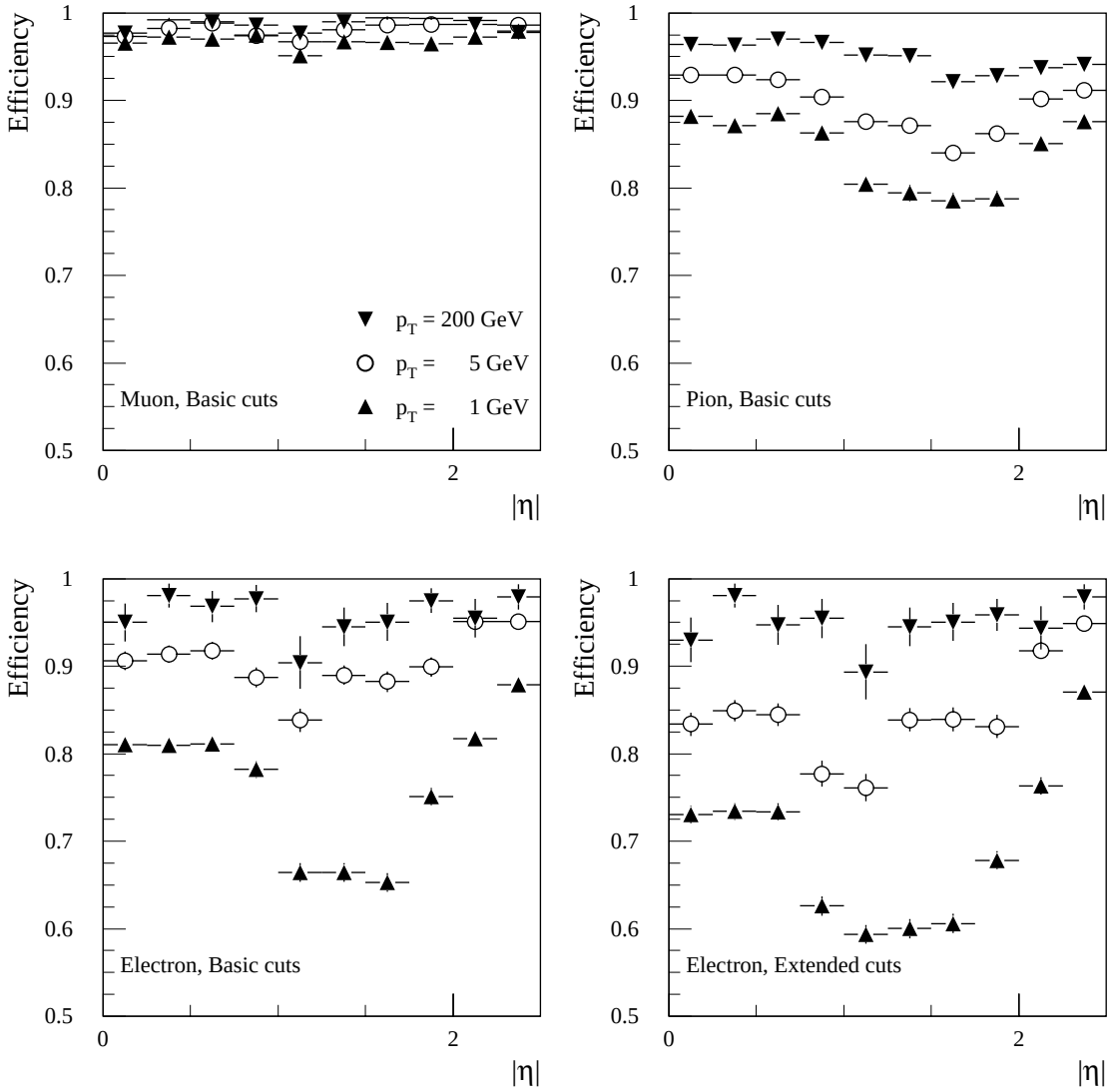

Figure 3-35 Track reconstruction efficiencies as a function of |η| for muons, pions and electrons with basic cuts and for electrons with extended cuts (see Section 3.1.3). Efficiencies are shown for tracks of p_T = 1, 5 and 200 GeV (xKalman).

$\Delta\eta\times\Delta\phi = 0.2\times0.2$). In practice the noise occupancy is expected to be $O(10^{-4})$ (see Figure 11-67 of [3-2]). However, should the noise increase, the thresholds will be raised to restore the low occupancy. Figure 3-37 shows the consequences of increased noise where the thresholds are set to four times the rms of the noise. It is clear from the figure, that by adjusting the threshold, the fake rate can be kept at an acceptable level without significant loss of efficiency. In the case that the detectors suffer significant radiation damage, the output signals will be reduced and the signal-to-noise ratio will need to be optimised more carefully. More details on the effect of noise in the SCT can be found in [3-16].

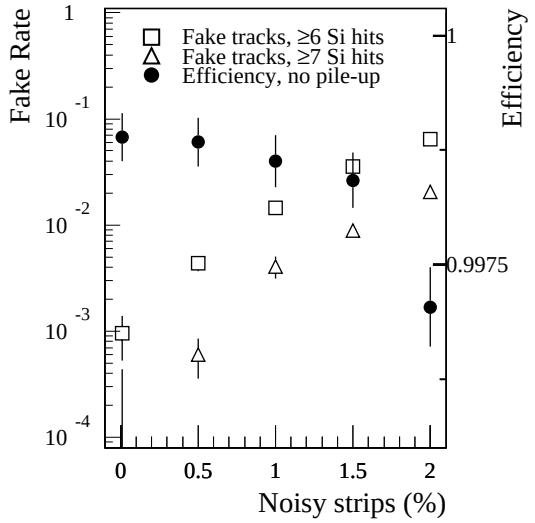

Figure 3-36 Fake rate in $\Delta\eta\times\Delta\phi = 0.2\times0.2$ ($p_T > 5$ GeV) and reconstruction efficiency ($p_T = 20$ GeV muons) as a function of the fraction of noisy strips in an SCT module (iPatRec).

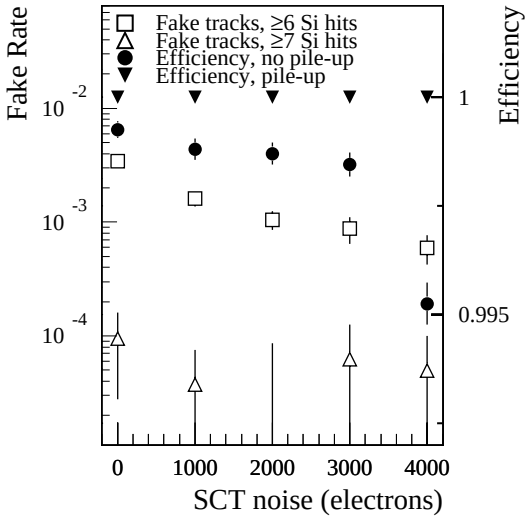

Figure 3-37 Fake rate in $\Delta\eta\times\Delta\phi = 0.2\times0.2$ ($p_T > 5$ GeV) and reconstruction efficiency ($p_T = 20$ GeV muons) as a function of the noise in the SCT strips (with a variable threshold) (iPatRec).

3.5.1.4 Effect of detector inefficiencies

Figure 3-38 shows the effect of reduced efficiency of the SCT strips, allowing for intrinsic efficiency, bonding faults, faults in the electronics *etc*. The pixel efficiency is held constant at 97%. The design SCT strip efficiency is ≥97%. It can be seen that the pattern recognition is fairly insensitive to variations in the SCT strip efficiency, although if the pixel efficiency is varied at the same time, it is found that there are significant losses arising from the insistence on a *B*-layer hit. In practice, should the efficiency of a module fall below ~90%, it may be replaced or removed from analysis by fiducial cuts. More details on the effect of inefficiencies in the SCT can be found in [3-16].

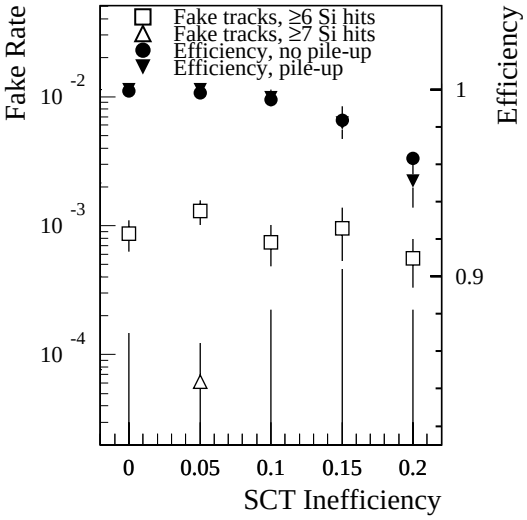

Figure 3-38 Fake rate in $\Delta\eta\times\Delta\phi = 0.2\times0.2$ ($p_T > 5$ GeV) and reconstruction efficiency ($p_T = 20$ GeV muons) as a function of the efficiency of SCT strips (iPatRec).

3.5.1.5 Effect of removal of layers

In an effort to reduce material in the ID, layouts with one less layer of silicon were examined [3-6]. These studies also served to highlight the consequences of large regions of the precision tracker becoming inefficient. Most of the emphasis was on *b*-tagging, as is discussed in Section 10.5.2. In a study of the electron efficiency after the LVL2 trigger, it was found that if one layer of silicon was removed, the efficiency resulting from the use of just the silicon could be maintained by adjusting the track cuts. However there was a ~40% increase in the background

rate from jets. If the TRT was included, then there was little degradation in the trigger performance. In a second study of K_s^0 reconstruction, it was estimated that if one SCT layer were removed, the acceptance would fall by ~5%.

3.5.1.6 Effect of misalignment

The targets for the alignment uncertainties of the ID detector elements are typically less than half of the intrinsic resolution of the devices (see Chapter 9 of [3-1]). To a large extent these should be achieved by surveying techniques and *in situ* monitoring. The alignment will be verified and improved by using tracks from *pp* collisions (see Section 3.7). To ensure that tracks can be found in the first place, the internal cuts used by the pattern recognition programs will need to be loosened. However, after an initial alignment has been completed, the remaining misalignments should be sufficiently small so as not to perturb the pattern recognition.

3.5.1.7 Recent changes to the pattern recognition programs

The ID pattern recognition programs have been undergoing continuous revision. Since the writing of the ID TDR and the studies reported above, the changes which have occurred have had the largest effects on the fake rates. In particular, xKalman was modified to give increased efficiency for conversion electrons and daughters of V^0's. This led to an increased fake rate when applying loose cuts on the number of precision hits. To compensate for this, additional quality cuts were applied for some recent studies. These cuts are: there should be no shared hits in the Precision Tracker, and the fit χ^2 should be less than 2 per degree of freedom.

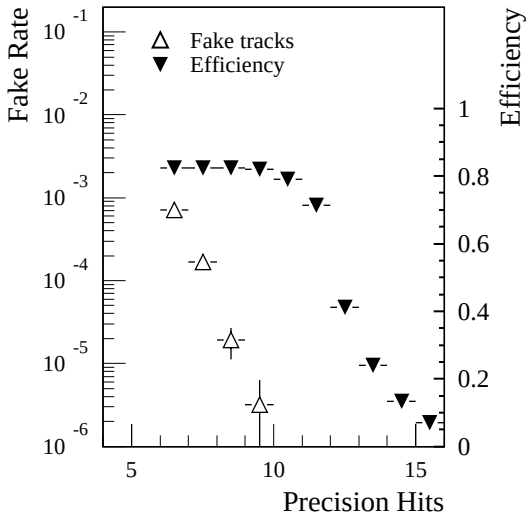

Figure 3-39 Fake rate in $\Delta\eta\times\Delta\phi = 0.2\times0.2$ ($p_T > 2$ GeV) and reconstruction efficiency ($p_T > 3$ GeV) as a function of the number of precision hits (6 to 15) (xKalman).

Figure 3-39 shows the fake rates and track finding efficiency as a function of the number of precision hits required on a track using the latest version of xKalman. The shape of the efficiency curve is similar to that shown in the ID TDR. However, the fake rate in a cone $\Delta\eta\times\Delta\phi = 0.2\times0.2$ falls more rapidly. Requiring at least six hits on a track leads to a fake rate of 7×10^{-4} compared to 3×10^{-4} reported in the ID TDR. However, requiring at least nine hits on a track leads to a fake rate of 3×10^{-6} compared to a rate of 3×10^{-5} reported in the ID TDR. Similar effects are seen for both xKalman and iPatRec in the *b*-tagging studies (see Section 10.2.2), where it is shown for the *b*-tagging cuts (at least nine precision hits), that the rate of fakes and secondaries is reduced using the latest programs, compared to the versions of the programs which were used for the ID TDR.

3.5.2 Tracks in jets

3.5.2.1 Basic results

Obviously the performance of the pattern recognition depends critically on the density of tracks in a jet, which in turn depends on the energy of the jet. Throughout the studies carried out recently, jets from 400 GeV Higgs bosons forced to decay to $q\bar{q}$ have been used to provide benchmarks. All tracks with $p_T > 1$ GeV and within a cone of $\Delta R < 0.4$ around the jet axis were analysed.

Figures 3-40 and 3-41 show respectively the reconstruction efficiency and the probability of fake tracks as a function of $|\eta|$ obtained by ASTRA (see Section 3.1.2). The effects of the material distribution are clear in these figures. The average track reconstruction efficiency over all $|\eta|$ is 87–90% and the average fraction of fakes is 0.1–0.4% – the ranges come from the comparison of different pattern recognition programs (see [3-6]). Figure 3-42 shows the reconstruction efficiency as a function of the distance from the jet-axis. The axis is determined from the initial *b*-quark direction – due to gluon radiation, this choice of axis causes the distribution to be smeared with respect to what would be seen with respect to the final quark direction. Figure 3-43 shows the efficiency as a function of the track p_T.

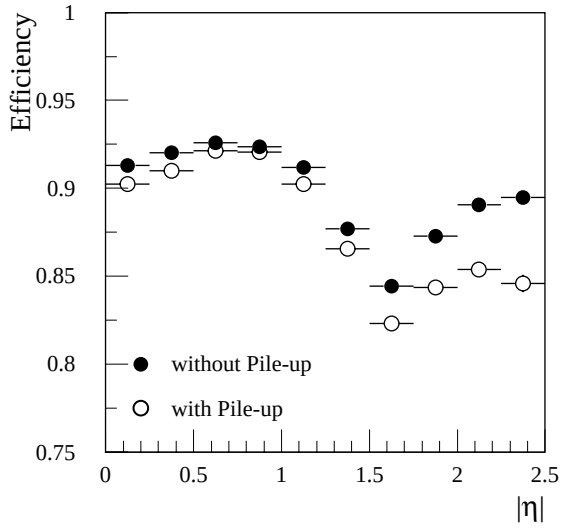

Figure 3-40 Track reconstruction efficiency as a function of pseudorapidity without and with pile-up at high luminosity for tracks in a jet (ASTRA).

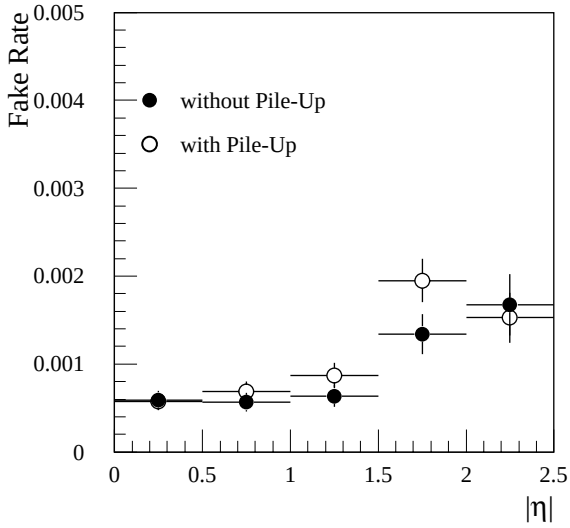

Figure 3-41 Fake rate as a function of pseudorapidity without and with pile-up at high luminosity for tracks in a jet (ASTRA).

3.5.2.2 Effect of pile-up and detector degradation

Table 3-3 shows a summary from [3-6] of the effect of various degradations on the pattern recognition performance. The consequences for *b*-tagging are discussed more extensively in Section 10.5. As well as basic efficiencies and rates, the fraction of tracks with bad hits (see [3-6] for definition) and the fraction in the tails (beyond $\pm 3\sigma$) are given. Those tracks in the d_0 tails can have a significant effect on the *b*-tagging performance. Along with the default conditions at low

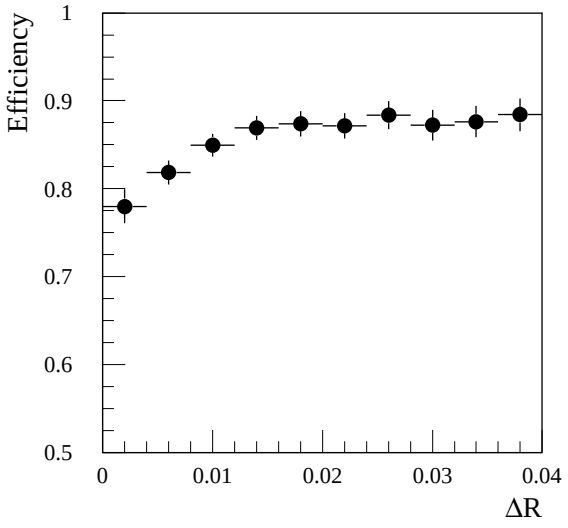

Figure 3-42 Track reconstruction efficiency as a function of distance from jet-axis for tracks in a jet (xKalman).

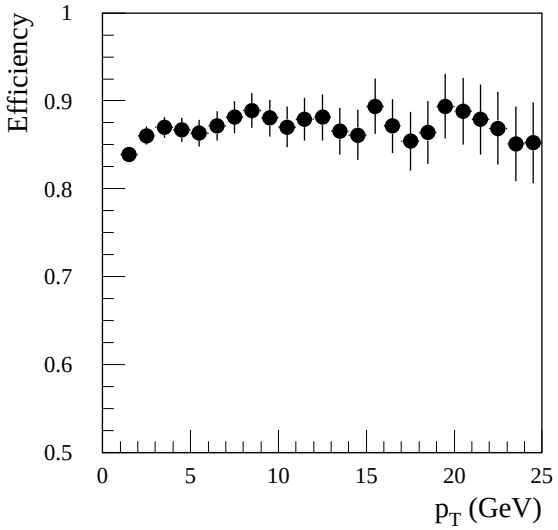

Figure 3-43 Track reconstruction efficiency as a function of track p_T for tracks in a jet (xKalman).

luminosity, the effects of pile-up at 10^{34} cm^{-2}s^{-1}, reduced silicon detector efficiency of 90% (default is 97%) and the effects of removing a middle layer of Pixels or the SCT have been considered.

It is not surprising that the effect of pile-up is not great, since the local occupancy arising from the tracks in jets of $p_T \sim 200$ GeV is typically three times that arising from pile-up tracks (see Tables 3-14 and 3-15 in [3-1]). Likewise, occupancy from noise hits is unlikely to be a problem since the pattern recognition problems are dominated by the proximity of tracks from the jet itself.

Table 3-3 Summary of the pattern recognition performance for tracks with $p_T > 1$ GeV in *u*-jets of $p_T \sim 200$ GeV (xKalman). The primary efficiency is the efficiency to reconstruct tracks belonging to the jet; the secondary rate is the fraction of reconstructed tracks coming from secondary interactions; the fake rate is the fraction of reconstructed tracks not associated with real particles. Results are shown for the default layout, with pile-up added at a luminosity of 10^{34} cm^{-2}s^{-1}, with reduced silicon efficiency and with silicon layers removed. More details can be found in [3-6].

	Default	**With pile-up**	**ε_{Si} = 90%**	**Remove Pixel layer**	**Remove SCT layer**
Primary efficiency (%)	89.5	87.7	83.9	89.3	89.0
Secondary rate (%)	3.3	3.5	3.1	3.6	3.7
Fake rate (%)	0.24	0.31	0.27	0.36	0.46
Tracks with bad Pixel hits (%)	4.7	5.1	4.9	8.2	4.9
Tracks with >20% bad Si hits (%)	2.3	3.8	3.6	5.9	4.6
Tracks in $1/p_T$ tails (%)	1.9	2.2	2.2	2.3	2.1
Tracks in d_0 tails (%)	1.9	2.1	2.4	3.2	2.0

Degrading the silicon efficiency to 90% has a significant effect on the reconstruction efficiency and on the d_0 tails. The ID is fairly robust to the loss of large regions of a single SCT layer, but the performance degrades significantly if a Pixel layer is lost. Of course, significant losses of modules in the *B*-layer would have dramatic effects for all physics related to displaced vertices.

3.5.3 Effect of improved TRT simulation

For all of the studies performed to date, including all those shown in this report, TRT hits from out-of-time beam-crossings have been treated as if they originated from in-time collisions (the standard simulation). In this section, the validity of this approximation is compared with what would be expected using the complete time-of-flight information.

3.5.3.1 Changes to the TRT digitisation

Details of the complete simulation can be found in Section 3.7.2 of the ID TDR. Since the time of the ID TDR, two improvements were made to the simulation of the TRT digitisation. Firstly, the energy dependence of the signal shape was included. Secondly, the TRT low threshold was modified to match the hit efficiency found in test-beam.

A new algorithm was implemented for the complete simulation, corresponding to what will be used in the TRT read-out electronics. The new algorithm is based on the fact that all tracks passing through a straw deposit some ionisation near the straw wall which causes the trailing edges of the output pulse to have a very narrow distribution in time (relative to the beam-crossing). The algorithm uses a gate which is 3 TDC bins (9 ns) wide to select this edge. This gate has the effect of considerably reducing the number of hits from out-of-time bunch-crossings which are seen by the pattern recognition programs when the time-of-flight information is used. The consequences for the complete method are that there is a larger chance of drift-time measurements being ‘shadowed’ by earlier pulses leading to bad or no drift-time information being recorded for a track.

3.5.3.2 Fake track study

A study of the fake track rate was undertaken to compare the standard pile-up method with the complete method using time-of-flight information (see Section 2.3.2). To examine the effect of the improved TRT simulation, xKalman was used because it is sensitive to the TRT digitisation by virtue of starting from the TRT hits using a fast histogramming method. A recent version of xKalman was used in the way described in Section 3.5.1.7. The fake rate was estimated in a cone $\Delta\eta\times\Delta\phi = 0.2\times0.2$ for tracks with $p_T > 2$ GeV. A corresponding track efficiency was found for ‘good’ tracks, *i.e.* tracks which were in-time, with $p_T > 3$ GeV and came from the minimum bias collisions.

Figures 3-44 and 3-45 show the fraction of drift-time hits found on good and fake tracks using the standard pile-up simulation and using the complete simulation respectively. To be considered, drift-time hits were required to be within $\pm2.5\sigma$ of the position expected from the fit to the complete track. There is a large difference between the distributions for good tracks compared to those for fakes. Comparing the different pile-up simulations, it can be seen that the mean number of drift-time hits is about 15% less using the complete simulation, since it provides a

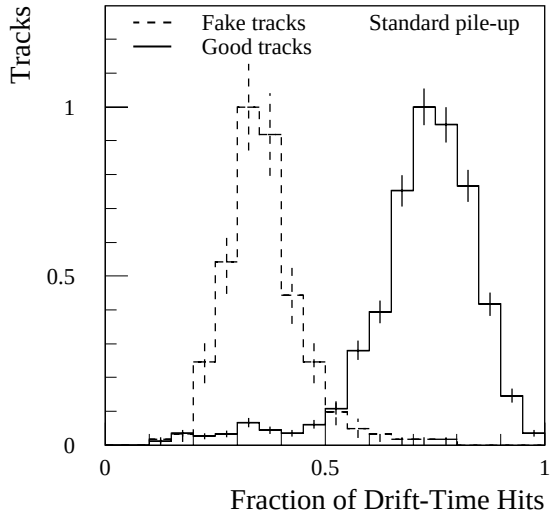

Figure 3-44 Fraction of drift-time hits for good tracks with p_T > 3 GeV and fake tracks with p_T > 2 GeV using the standard pile-up method. All tracks are required to have ≥6 precision hits. The normalisation is arbitrary.

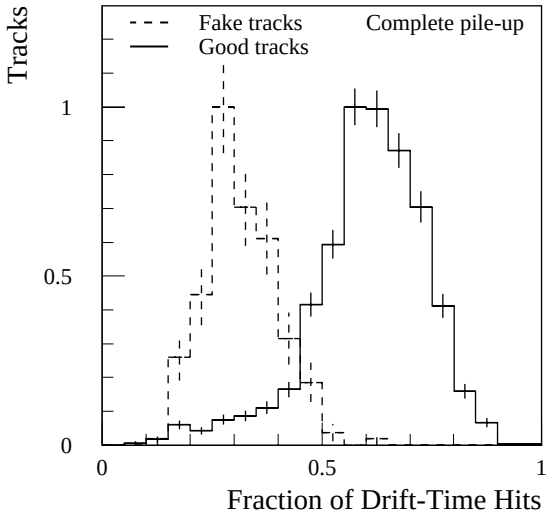

Figure 3-45 Fraction of drift-time hits for good tracks with p_T > 3 GeV and fake tracks with p_T > 2 GeV using the complete pile-up method, incorporating time-of flight information. All tracks are required to have ≥6 precision hits. The normalisation is arbitrary.

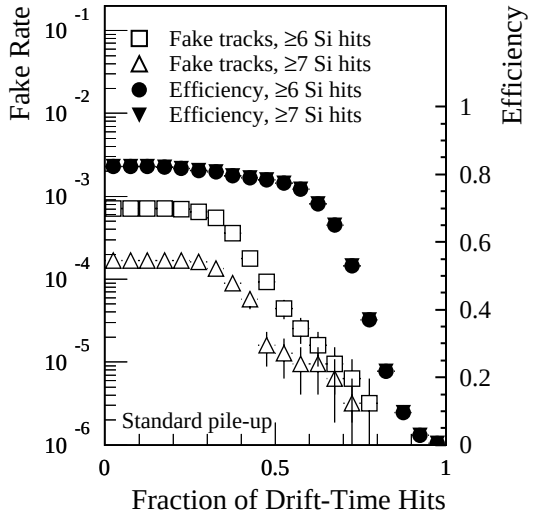

Figure 3-46 Fake rate in $\Delta\eta\times\Delta\phi = 0.2\times0.2$ (p_T > 2 GeV) and reconstruction efficiency (p_T > 3 GeV) as a function of the fraction of drift-time hits (xKalman). Distributions correspond to standard pile-up simulation.

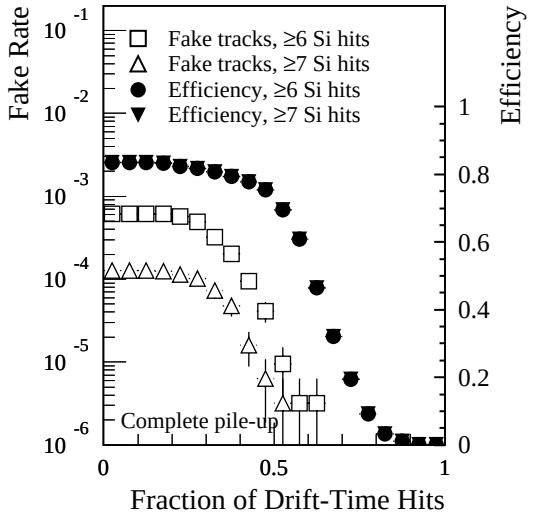

Figure 3-47 Fake rate in $\Delta\eta\times\Delta\phi = 0.2\times0.2$ (p_T > 2 GeV) and reconstruction efficiency (p_T > 3 GeV) as a function of the fraction of drift-time hits (xKalman). Distributions correspond to complete pile-up simulation using time-of-flight information.

better description of the shadowing of the hits of interest by earlier pulses. Nevertheless, the total number of straw hits found on a track (regardless of whether a leading edge can be identified or not) changes by only about 3%.

Figures 3-46 and 3-47 show the track finding efficiencies and fake rates using the standard pile-up simulation and using the complete simulation respectively. Tracks are found with a slightly higher efficiency (1.5%) in the complete pile-up sample because it is possible to use the narrow gate level gate to exclude out-of-time hits. The fake rates generated by the complete pile-up

method are ~20% lower than using the standard method. Some of the reduction in fake rate may be partially as a result of the reduced number of valid drift-time hits. Using the complete method, both the fake rate and efficiency fall off more rapidly as a function of fraction of drift-time hits than they do using the standard pile-up method.

3.5.4 The effect of the solenoidal field

The analytic calculations of Section 3.3.1 indicate that the reduced magnetic field in the outer regions of the ID will lead to reduced track parameter resolution, especially in the case of the transverse momentum. However, to first order, no degradation in the performance of the pattern recognition is expected since the hit density will be little changed.

xKalman has been upgraded from Fortran to C++ and allowance has been made for the non-uniform *B*-field which is created by the solenoid. The improved program uses Runge-Kutta extrapolation techniques and, despite the added complexity, is only a factor of 1.5 slower than the Fortran version for a uniform field.

3.5.4.1 Track reconstruction

It is essential to allow for the field non-uniformities when reconstructing tracks, otherwise momenta will be overestimated. If a particle is tracked through the solenoidal field, but reconstructed as if the field were uniform, the shift in $1/p_T$ is a strong function of pseudorapidity, varying between +5% ($|\eta| < 1$) and −10% ($|\eta| > 2$) for p_T's in the range 1 to 20 GeV. Figure 3-48 shows the fractional difference between the reconstructed and true values of $1/p_T$ as a function of $|\eta|$ when allowance is made correctly for the solenoidal field. The means are systematically displaced from zero with an average over $|\eta| \leq 2.5$ of (0.14 ± 0.02)%. However, this is much less than if the field were assumed incorrectly to be uniform in the reconstruction. Similar effects to those seen in Figure 3-48 are seen with simulations made with a uniform field. Furthermore, the shape as a function of $|\eta|$ is similar to that of the material distribution (see Figure 3-5), suggesting that their may still be some effects related to the material and *dE/dx*. Work is continuing in this area in order to remove the remaining biases.

Figure 3-49 shows the comparison of the resolutions obtained with the solenoidal and uniform field. The superimposed line is derived from the ratio of the corresponding curves taken from Figure 3-8. It can be seen that the analytic calculation provides a reasonable description of the effects of the non-uniform field. Allowance has been made for the fact that inside the ID cavity, the field will be enhanced by ~5% due to the presence of the iron of the Hadronic Calorimeter.

3.5.4.2 Pattern recognition

If no allowance is made for the fact that particle trajectories in the solenoidal field are different from helices (even allowing for multiple scattering), then there is the likelihood of missing hits on a track and hence of a reduced track efficiency. For p_T = 20 (1) GeV muons tracked through a solenoidal field, but reconstructed as if the field were uniform, the reconstruction efficiency is 95 (82)% to be compared with 98 (97)%, as seen from Table 3-2 corresponding to simulation with a uniform field. However, if allowance is made correctly for the field, there is no difference between the efficiency found in the case of the solenoidal field compared to the case of a uniform field. This confirms that the pattern recognition in the non-uniform field can be undertaken with no loss of performance.

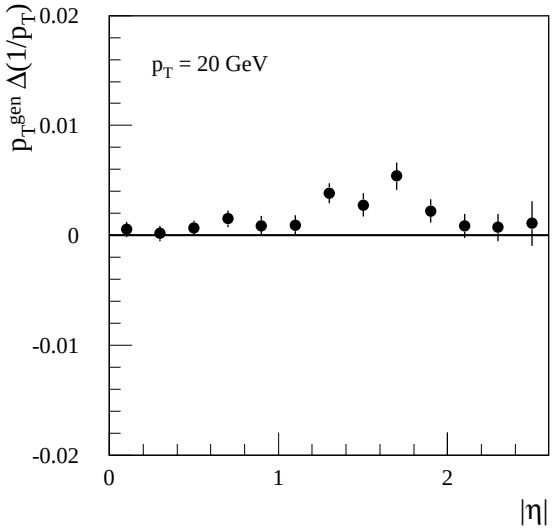

Figure 3-48 Fractional difference between reconstructed and true $1/p_T$ for single 20 GeV muons in a solenoidal *B*-field as a function of pseudorapidity.

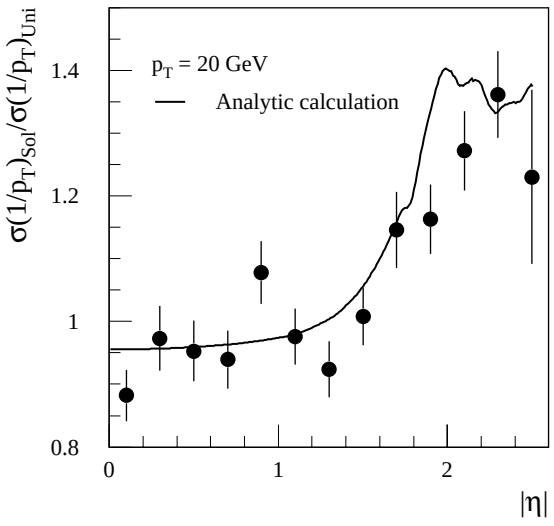

Figure 3-49 Ratio of resolution obtained with a solenoidal field to that with a uniform field for 20 GeV muons. Superimposed is the analytic calculation.

Reconstructing electron tracks is more difficult than muons since the field causes an electron after bremsstrahlung to deviate from the original trajectory. This effect will be reduced in a weaker field. Hence, electron reconstruction should be no more difficult with the solenoidal field than with a uniform one. Further, the difference between the associated calorimeter cluster and the electron impact point in the calorimeter will be less, which will be advantageous for the calorimetric energy measurement.

3.6 Vertex reconstruction

3.6.1 Primary vertex reconstruction

At the LHC, the beam-spot will be described by Gaussian parameters: $\sigma_x = \sigma_y = 15\,\mu m$ and $\sigma_z = 5.6$ cm. For most analyses, this information (especially that in the transverse plane) is already sufficient, but for some analyses, a better knowledge of the position of the primary vertex is desirable.

In Section 6.4 of the ID TDR [3-1], it was shown how, at low luminosity, it is possible to determine the position of the primary vertex on an event-by-event basis by an iterative procedure which tries to fit all the reconstructed tracks to a common vertex, removing at each step those tracks which look inconsistent with the hypothesis that they come from the primary vertex (secondaries from interactions, particles with a lifetime and mismeasured tracks). With this procedure, the primary vertex position resolution becomes basically a function of the total number of tracks (and of their quality) which can be successfully attached to the same vertex. The fitting procedure was found to improve the transverse resolution only for high track-multiplicity events (more than 30 tracks in the primary vertex fit, as in $H \rightarrow b\bar{b}$ events with $m_H = 400$ GeV). Additional improvements can be obtained by combining this method with some other inde-

pendent estimate of the transverse position of the primary vertex, such as the beam-spot position determined on a run-by-run basis (as done in some of the LEP experiments and in CDF [3-17]), by using the d_0-ϕ correlation of the tracks in the event.

Significant improvements in the *z*-position measurement can be achieved: a resolution in the range 22–50 μm (although with some non-negligible tails) for track multiplicities ranging between 10 and 36. These figures are well inside the ATLAS physics requirements of 1 mm for the resolution of the *z*-coordinate of the primary vertex [3-18]. A summary of the results for low luminosity is shown in Table 3-4.

Table 3-4 Widths of residual distributions for position measurements of the primary vertex (transverse and longitudinal) for various samples of physics events at low luminosity. The Gaussian widths of the core and the rms's are given.

	σ (μm)		rms (μm)	
Sample	***x* or *y***	***z***	***x* or *y***	***z***
Minimum bias	31	49	59	72
$H \rightarrow \gamma\gamma$, $m_H = 100$	22	41	32	49
$H \rightarrow b\bar{b}$, $m_H = 400$	10	22	14	27
$B_d \rightarrow J/\psi K_s$	23	35	38	50
$B_s \rightarrow D_s\pi$	23	38	39	51

At high luminosity, the problem of multiple interactions in the same bunch-crossing needs to be addressed. An average of 24 minimum bias pile-up events are expected to be superimposed on a signal event in the Inner Detector. In principle, it is necessary to reconstruct only the signal event, and in some cases, this could be identified easily because minimum bias events will have a smaller charged track multiplicity and a smaller total transverse momentum. Unfortunately this is not always true and in some analyses, the selection of the signal event based on these selection criteria might introduce dangerous biases. Therefore, it would be preferable to reconstruct as many as possible of the primary vertices in an event and leave the identification of the primary vertex of the signal event for later in the analysis chain when more sophisticated information is available (including the presence of leptons, photons, jets, *b*-jets, τ's, *etc*.).

A generalisation of the algorithm used in the low luminosity case has been developed [3-14]. In a first step the algorithm assumes that all tracks are coming from the beam-line in the transverse plane (this is a good approximation due to the small transverse beam-spot size) and determines the *z*-coordinate of each track. Each of these values constitutes an entry in a histogram with a 500 μm bin size. This histogram is then scanned to look for locations where the tracks cluster as they should do if they are coming from the same vertex. A minimum of four tracks is required to define a cluster. For each cluster, the corresponding tracks constitute the input to the same algorithm used at low luminosity. If the fit is successful, the vertex is retained.

The algorithm was applied to a sample of $H \rightarrow \gamma\gamma$ events with $m_H = 100$ GeV. Reconstructed charged tracks were selected using the same quality cuts described in Section 6.4 of the ID TDR; the only difference was that a higher track p_T threshold (1 GeV instead of 0.5 GeV) was applied.

In Figure 3-50, an example of the histogram of the *z*-coordinate of the tracks for one beam-crossing is shown. The *z*-coordinate of the reconstructed tracks (bottom) is compared to the distribution of the *z*-coordinate of particles (top). The arrow on the upper histogram indicates the signal event. In this example, it can be seen that the signal event is associated with the cluster which has the highest track multiplicity, however, this is not always true.

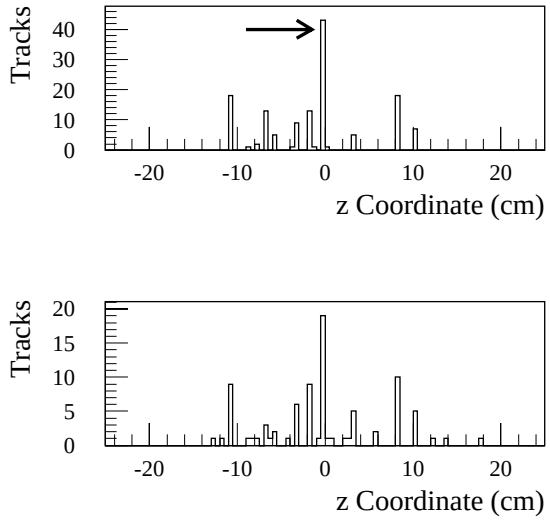

Figure 3-50 Distribution of the intersection of the tracks with the *z*-axis for one particular beam-crossing at high luminosity at particle level (top) and after reconstruction (bottom). The arrow indicates the $H \rightarrow \gamma\gamma$ vertex.

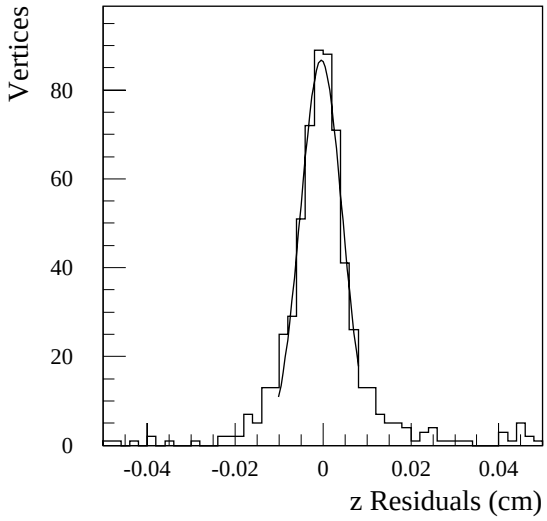

Figure 3-51 Residuals on the *z*-measurement of the primary vertex for $H \rightarrow \gamma\gamma$ with pile-up. Superimposed is a Gaussian fit to the core of the distribution.

On average, the algorithm reconstructs five primary vertices at high luminosity. This number is considerably lower than the ~25 vertices present in one beam-crossing. This difference is due to track losses resulting from the 1 GeV p_T cut as well as the fact that some of the vertices merge. With a requirement of a minimum of two tracks to define the primary vertex, the primary vertex of the signal event is found in the list of reconstructed vertices 72% of the time. The *z*-resolution is about 48 μm with an rms of 106 μm, compared to values of 41 μm and 49 μm, respectively, observed on the same sample at low luminosity. The residual distribution for the *z*-coordinate of the reconstructed primary vertices is shown in Figure 3-51.

3.6.2 Secondary vertices

3.6.2.1 V^0 reconstruction

The reconstruction of the decay $K_s^0 \rightarrow \pi^+\pi^-$ was studied in Section 6.5 of [3-1]. The reconstruction of such decays is difficult due to the long lifetime of the K_s^0, which leads to tracks with reduced numbers of silicon hits and large impact parameters.

The previous studies were performed using single K_S^0's of fixed p_T (3, 5 and 7 GeV), distributed uniformly in the interval $|\eta| \leq 2.5$. Due to the importance of K_S^0 reconstruction for B physics and, in particular, for the decay $B_d^0 \rightarrow J/\psi\, K_S^0$ (see Section 17.2.2), the reconstruction has now been studied in the context of B_d^0 decays (in the absence of pile-up).

The analysis was performed using 15,000 $B_d^0 \rightarrow J/\psi\, K_S^0$ events generated with PYTHIA and fully simulated using GEANT. The average p_T of the K_S^0's was 4.7 GeV. Charged tracks were reconstructed using xKalman, down to a minimum p_T of 0.5 GeV for $|\eta| \leq 2.5$. The analysis was similar to that performed previously, except that a minimum of six precision hits was required. This choice allowed the reconstruction of K_S^0's up to a decay radius of 37 cm in the barrel region. The algorithm for finding K_S^0's looped on all pairs of oppositely charged tracks in the event and fitted them in 3D to a common vertex. It was required that the χ^2 per degree of freedom be less than six. Pion masses were assigned to both tracks and the invariant mass calculated. Track pairs were retained if the invariant mass was within $\pm 3\sigma$ of the nominal K_S^0 mass. Finally, to reduce the prompt track background, the reconstructed transverse decay radius of the K_S^0 candidate was required to be greater than 1 cm.

To be compatible with the sin(2β) analysis, all events were subjected to all trigger and selection cuts used in the B_d^0 analysis to reconstruct a J/ψ. The cuts used to select K_S^0 candidates effectively defined a fiducial region inside the ID in which decays could be reconstructed: $1 < R < 37$ cm and $|z| < 210$ cm. The K_S^0 reconstruction efficiency was defined as the fraction of events with a reconstructed J/ψ where the true K_S^0 from the B_d^0 decay was correctly reconstructed and satisfied the various selection cuts. The total efficiency is 41.1% which includes: the acceptance for K_S^0's with a decay inside the fiducial region of 68.6%, the xKalman reconstruction efficiency for the two pion tracks of 76.9% and the effect of cuts on reconstructed K_S^0 candidates of 77.8%. If the cut on the number of precision hits is relaxed to four, then the corresponding efficiencies are: 41.4% (total) and 73.4%, 74.9% and 75.3% respectively – the acceptance is increased but the quality of the reconstruction is decreased. This definition of efficiency is different from that used in [3-1] but more useful for the studies of Section 17.2.2, since in the ID TDR, the efficiencies were normalised to decays with $1 < R < 44$ cm for which the tracks were reconstructed. The total reconstruction efficiency is shown as a function of the K_S^0 decay radius and of the K_S^0 pseudorapidity in Figures 3-52 and 3-53, respectively. The reconstruction efficiency falls from a maximum of 70% where the decay is in the Pixel volume to close to zero at the outer radius of the fiducial volume where pions, even if they can be reconstructed, fail the selection cuts. It can be seen that there is a dip in the efficiency as a function of the K_S^0 pseudorapidity in the overlap region between the barrel and the end-cap.

Figures 3-54 and 3-55 show the mass and decay radius resolution as a function of the decay radius. The mass resolution varies between 4.5 and 7 MeV in the fiducial volume. It is affected mainly by the reconstruction of momenta and angles which are well determined by the tracking layers beyond the decay vertex and hence are less sensitive to the position of the decay. As expected, the decay radius resolution depends strongly on the radius of the decay and is much better for decays just in front of the Pixel layers, but is worse for decays inside the SCT, which has poorer $R\phi$ resolution, especially in the absence of R-z measurements from the Pixels.

3.6.2.2 Lifetime measurements

Measurements of vertices displaced by O(1) mm from the primary vertex will be essential for B physics (see Chapter 17), b-tagging (for example $H \rightarrow b\bar{b}$) (see Chapter 10) and lifetime measurements. In the Pixel TDR [3-3], it was shown that a resolution of the proper time of 0.073 ps could be obtained – this is discussed more in Section 17.3. It may be possible for ATLAS to make

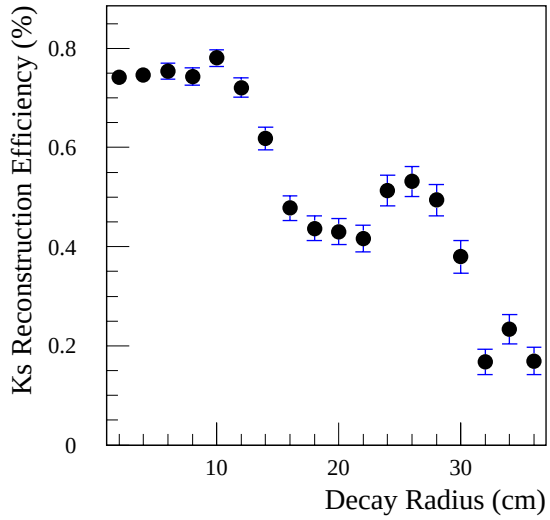

Figure 3-52 K_s^0 reconstruction efficiency as a function of decay radius.

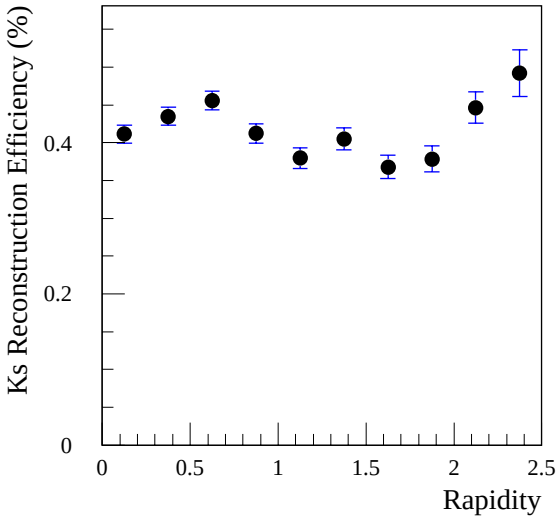

Figure 3-53 K_s^0 reconstruction efficiency as a function of |η|.

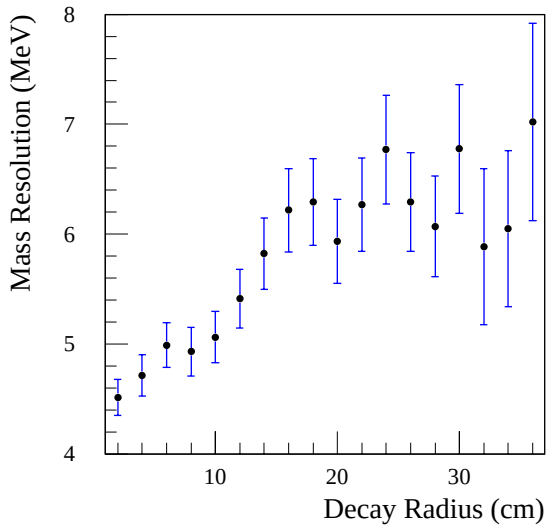

Figure 3-54 K_s^0 mass resolution as a function of decay radius.

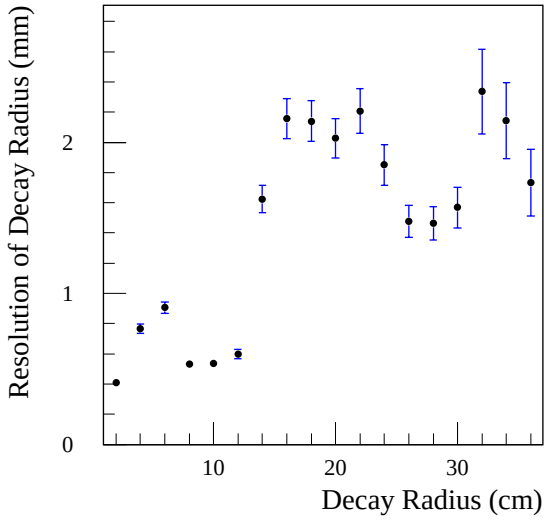

Figure 3-55 Resolution of K_s^0 decay radius as a function of decay radius.

useful measurements of the τ lifetime. Although the ID will be essential for this, the use of the calorimetry to determine the τ momentum will be critical in order to obtain the proper lifetime distributions. This is discussed more in Section 9.3.3.3.

3.7 Alignment

In the ID TDR, the targets for the alignment were such that misalignments should degrade the track parameter resolutions by no more than 20%. This led to requirements that in $R\phi$, the Pixel detectors should be aligned to ~7 μm, while the SCT detectors should be aligned to ~12 μm. The desire to measure the W mass to 20 MeV (see Chapter 16) will necessitate knowing the momentum scale measured by the Inner Detector to ~0.02%. This level of precision will be attained by

calibrating with the Z mass (see Chapter 12). Nevertheless, to be able to control the systematics sufficiently well will require a very good understanding of the alignment. It is plausible that this may require understanding the alignment of detectors in $R\phi$ at the level 1 μm, although this value is very difficult to justify. Achieving this accuracy may seem unrealistic, however it may be sufficient to consider averages in intervals of space and time. Further requirements on the ID motivated by a W mass measurement are discussed in Section 12 and in more detail in [3-19].

Information on alignment of the Inner Detector will come from: the metrology of individual modules at the time of construction, the system tests of sets of modules, surveys of the completed barrels and wheels (in particular, from the X-ray survey), and the Frequency Scan Interferometry (FSI) which measures a network of lengths *in situ* on the SCT. This information will be used to provide a starting point for the offline alignment using physics events. More details can be found in Chapter 9 of [3-1].

3.7.1 Strategy

The alignment of the ID will inevitably start in the Precision Tracker (Pixels and SCT). After an initial alignment to ensure that tracks can be reconstructed with reasonable efficiency, the alignment between neighbouring modules within single barrels and wheels will be performed using tracks of modest momentum passing through the overlaps. To correct more complex misalignments such as the translation and rotation in 3D of modules and global distortions such as rotations of complete units and radial distortions (*e.g.* elliptical ones), stiffer tracks crossing the complete ID will be needed. In principle, all alignment constants might be determined in a single pass by solving a very large matrix equation, as has been done by ALEPH [3-20] and SLD [3-21]. However, because the ID is so complicated, a great deal of iteration will be needed to accommodate related information. Some effects, such as thermal distortions, have the potential to mask smaller systematics. These will need to be understood by combining data from different runs so that such effects can then be parametrised, for example, as a function of measured temperature or luminosity. This would then allow some systematics to be factorised out of the alignment problem at some level. Having understood the Precision Tracker, the TRT can then be investigated.

3.7.2 Study of alignment in the Precision Tracker

Specialised triggers for alignment are foreseen in the trigger menus (see Section 11.2.6), however these are not considered here. To start to understand the potential for aligning the ID, a study [3-22] was made using single muons of different p_T (45, 6 and 2 GeV), distributed uniformly in $|\eta| < 2.5$. The momenta were chosen to be characteristic of muons from $W \rightarrow \mu\nu$, 6 GeV muons which provide triggers for B physics and lower energy particles in triggered events. It is important to allow for multiple scattering when fitting a track in the ID, however, in fitting the scattering angles at each silicon plane, there is a tendency for the fitted track to be pulled strongly by each hit and to minimise the residuals unrealistically, especially at low p_T. Therefore, the residuals between the track fit and the reconstructed hit position on each silicon plane were found by fitting the tracks in the rest of the Precision Tracker with iPatRec, but excluding that plane.

Figure 3-56 shows the width of the $R\phi$ residuals in the middle Pixel barrel. At high momentum, these are a bit larger than the intrinsic resolution (16 μm vs 11 μm). At lower momenta, the residuals are inflated by multiple scattering which increases with $|z|$. The jump around $|z| = 30$ cm comes from falling off the outer pixel barrel and picking up hits on the first pixel

disk. Figure 3-57 shows the width of the $R\phi$ residuals in the middle pixel barrel using the $R\phi$ overlaps. The residuals in the overlaps were found from the difference in the residuals of one module and the overlapping module and are much less sensitive to multiple scattering. The widths should be close to $\sqrt{2}$ times the intrinsic resolution, *i.e.* about 15 μm. It can be seen that there is an oscillatory behaviour as a function of z. This arises since the distributions of the differences of the residuals are not Gaussian but show some signs of the discrete nature of the pixel measurements.

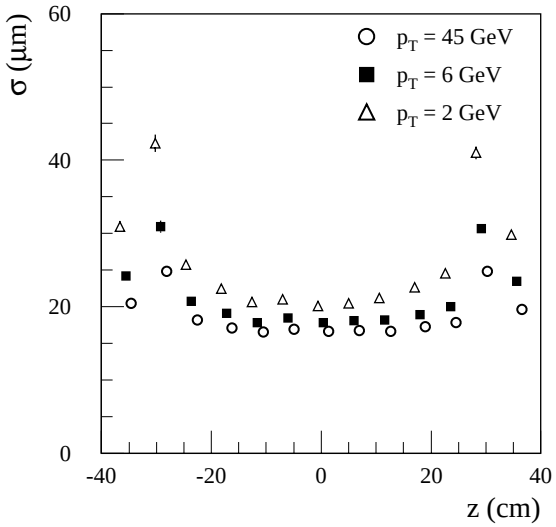

Figure 3-56 Width of $R\phi$ residual distributions in modules of the middle pixel barrel layer as a function of the position of the module. (Points are offset horizontally to avoid overlapping.)

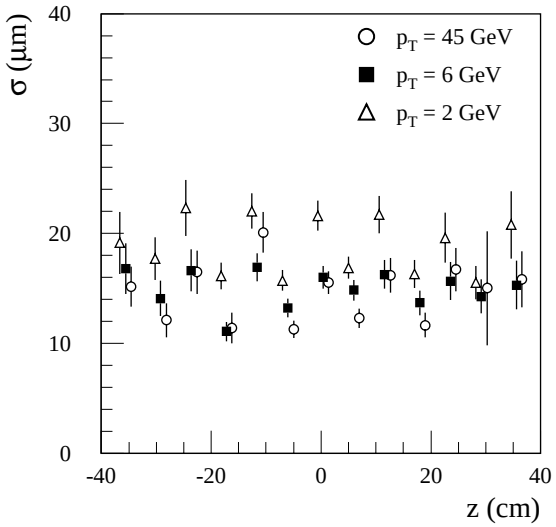

Figure 3-57 Width of $R\phi$ residual distributions using R-ϕ overlaps in the middle pixel barrel layer as a function of the position of the module. (Points are offset horizontally to avoid overlapping.)

Figures 3-58 (barrels) and 3-59 (end-cap disk and wheels) show the widths of the $R\phi$ residuals in the various pixel and SCT layers. The widths were found from the residual distributions for all hits in a given layer. The residuals in the SCT are typically twice as large as those in the Pixels, reflecting the difference in the intrinsic resolutions: 11 μm vs 22 μm. The averaged residuals in the B-layer are much larger than in the other pixel layers because there are no constraints at lower radii (the same effect is seen in outer SCT barrel) and the modules at large $|z|$ are hit at small angles of incidence leading to large multiple scattering at lower p_T. The residuals seen in the end-caps are comparable to those in the barrel.

The alignment precision which can be achieved after one day of running at low luminosity was derived from the widths of the residual distributions shown in Figures 3-58 and 3-59 and the expected rates. Alignment between layers was studied assuming muons from $W \rightarrow \mu\nu$ and $p_T \geq 6$ GeV muons (from the B physics sample) can be used. Alignment within layers requires tracks crossing the overlaps with higher rates to compensate for the smaller solid angle. Since multiple scattering is less important, it was assumed that $p_T \geq 6$ GeV muons and all particles (predominantly pions) with $p_T \geq 2$ GeV in triggered events could be used. Assuming events triggered by $p_T \geq 6$ GeV muons for B physics will be reasonably characteristic of any triggered events, it was found that each event had 10 particles with $p_T \geq 2$ GeV in the absence of pile-up. For the three types of tracks ($W \rightarrow \mu\nu$, $p_T \geq 6$ GeV muons and all particles with $p_T \geq 2$ GeV) the residuals from the three muon samples (p_T = 45, 6 and 2 GeV) were assumed. The corresponding rates at peak luminosity were assumed to be 3 Hz (after triggering and all cuts), 50 Hz (where the $p_T \geq 6$ GeV muon trigger is assumed to take half of the available DAQ bandwidth)

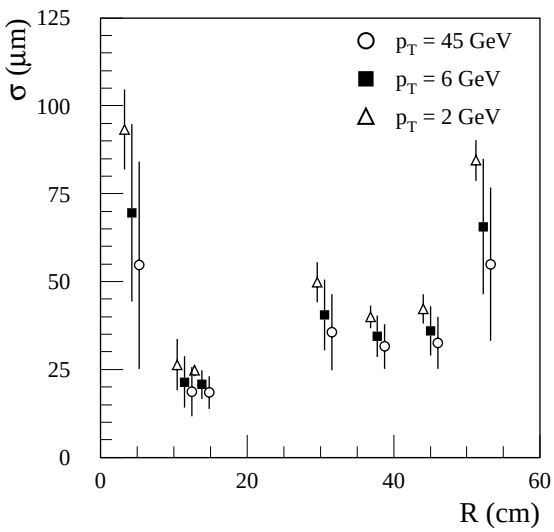

Figure 3-58 Width of $R\phi$ residual distributions in barrels layers, averaged over the complete layer, as a function of the position of the layer. The 'error bars' indicate the spread of measurements from different modules in the same layer. (Points are offset horizontally to avoid overlapping.)

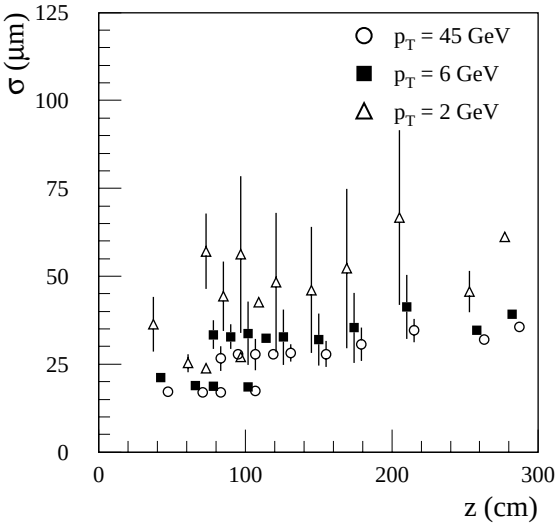

Figure 3-59 Width of $R\phi$ residual distributions in endcap layers, averaged over the complete layer, as a function of the position of the layer. Note that the last pixel disks are at similar positions in z to the first SCT wheels. The 'error bars' indicate the spread of measurements from different modules in the same layer. (Points are offset horizontally to avoid overlapping.)

and 10×100 Hz (allowing for 10 tracks in every event). It was assumed that the running time in one day would be 2×8 hours and that for $W \rightarrow \mu\nu$, the rate of which is limited by the luminosity, a 60% efficiency should be used to allow for the luminosity lifetime. These two effects were accounted for by a scale factor. To make the calculations transparent, a 1% $R\phi$ overlap of the sensitive area for all modules has been assumed (that is 1% on each edge of each module).

The calculations are illustrated for the middle Pixel barrel in Table 3-5, which shows the precision which can be obtained for the $R\phi$ alignment after one day of low luminosity running – more details can be found in [3-22]. A summary of the precisions which can be obtained for the different barrel layers using all the hits in a module is shown in Figure 3-60. The 'error bars' show the spread of the values for the different modules of a given layer arising from different rates and residual distributions. Figure 3-61 shows the precision which can be obtained in the Pixel barrel layers using the overlaps. The results are summarised in Table 3-6. For the averages in the first column (precision for Pixel barrels using complete modules), the *B*-layer was excluded because of the large variations in the precision arising from modules at large $|\eta|$.

Table 3-5 Components of the calculation of the alignment precision in $R\phi$ which can be obtained in the middle Pixel barrel after one day of low luminosity running. See text for more details.

Type of track	Rate (Hz)	Scale fact	Width of resid. (μm)		Precision (μm)	
			Module	Overlap	Module	Overlap
$W \rightarrow \mu\nu$	3	0.4	19	17	0.9	
Single muons, $p_T \geq 6$ GeV	50	0.66	21	19	0.3	2
Low-p_T tracks, $p_T \geq 2$ GeV	10×100	0.66	26	27		0.8

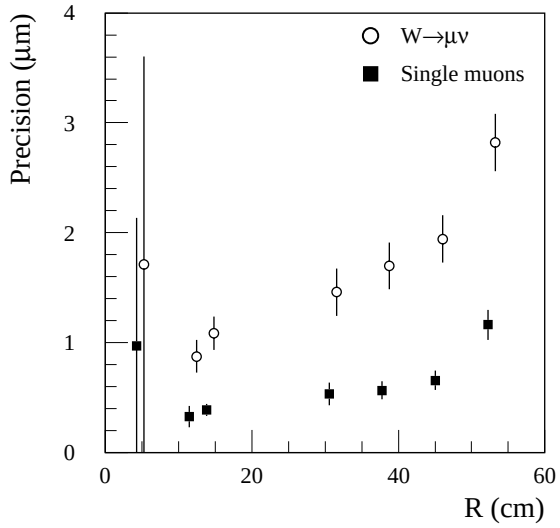

Figure 3-60 Precision which can be achieved after one day of low luminosity running for the $R\phi$ alignment of barrel modules as a function of the position of the layer. Results are shown for different types of tracks — see text for more details. The 'error bars' indicate the spread of measurements from different modules in the same layer. (Points are offset horizontally to avoid overlapping.)

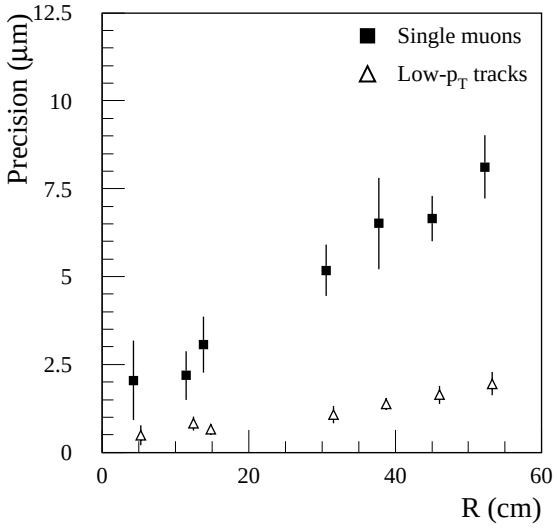

Figure 3-61 Precision which can be achieved after one day of low luminosity running for the $R\phi$ alignment of barrel modules using the $R\phi$ overlaps as a function of the position of the layer. Results are shown for different types of tracks — see text for more details. The 'error bars' indicate the spread of measurements from different modules in the same layer. (Points are offset horizontally to avoid overlapping.)

Table 3-6 $R\phi$ alignment precisions (μm) which can be obtained after one day of low luminosity running. Results are given for different types of tracks, using both complete modules and the $R\phi$ overlaps.

Type of Track	Pixels				SCT			
	Barrel		End-cap		Barrel		End-cap	
	Module	Overlap	Module	Overlap	Module	Overlap	Module	Overlap
$W \rightarrow \mu\nu$	1.0		1.2		2		1.3	
Single muons	0.4	2.4	0.4	4	0.7	7	0.5	5
Low-p_T tracks		0.7		0.9		1.5		1.0

From Table 3-6, it would seem that at low luminosity it should be possible to align the Precision Tracker to O(1) μm in one day using tracks crossing the complete detector (anywhere in a module) or using the overlaps (assumed to be 1%). The information provided by the overlaps is complementary to that provided by the complete detector and will be sensitive to different systematics. These conclusions must be qualified by several effects which are potentially more significant than some of the steps made in these calculations. There are uncertainties in the cross-sections and efficiencies (trigger and reconstruction) for the different types of tracks which have been considered and in the actual luminosities which will be delivered. The alignment needs to be done in 3D (each module having six degrees of freedom), which may degrade the results of the naive calculations. In addition, there will be other sources of systematics which will need to be understood and these may be greater than 1 μm. The $p_T \geq 6$ GeV muons used to trigger B physics events may be contaminated by π/K decays and such tracks may not be good for alignment. Nevertheless, at the LHC, it is certain that there will be many low-p_T tracks which

will be valuable for alignment with the overlaps and sufficient high-p_T tracks for more global alignment. It would seem that the statistical precision which can be obtained using track-based alignment will allow the more complex systematics in the ID to be studied and corrected.

3.8 Conclusions

Since the ID TDR, the largest changes to the layout have occurred in the Pixel System. Nevertheless, because the intrinsic detector resolutions have not changed significantly and the philosophy of providing at least three pixel measurements on tracks ($|\eta| \leq 2.5$) has been maintained, to a large extent, the expected performance presented in this report is similar to that found at the time of the ID TDR. After two years of refining the engineering design, the material in the active region of the ID has increased by about 5% X_0 to ~48% X_0.

The track resolutions for muons can be described approximately by:

$$\sigma\left(\frac{1}{p_T}\right) \approx 3.6 \times 10^{-4} \oplus \frac{1.3 \times 10^{-2}}{p_T \sqrt{\sin\theta}} \quad (\mathrm{GeV}^{-1})$$

$$\sigma(d_0) \approx 11 \oplus \frac{73}{p_T \sqrt{\sin\theta}} \quad (\mu\mathrm{m})$$

where p_T is in GeV. The effects expected for a solenoidal field have been confirmed using full simulation: there is little change in the $1/p_T$ resolution in the barrel, but at higher pseudorapidity, the resolution degrades, becoming 40% worse at $|\eta| = 2.5$. Nevertheless, good charge determination is maintained up to $p_T = 1$ TeV where the misidentification probabilities are <2% and <5% for muons and electrons respectively.

Systematic comparisons have been made between muons, pions and electrons. While the distributions of reconstructed track parameters of pions are similar to those of muons, electrons suffer from bremsstrahlung. At high momenta, muons can be reconstructed with 99% efficiency, which is limited by the track quality cuts; pions and electrons can be found with efficiencies around 95%. For $p_T = 1$ GeV, the efficiencies to find and reconstruct isolated muons, pions and electrons are 97%, 84% and 76% respectively. These efficiencies are fairly robust to the effects of detector inefficiency and noise as well as pile-up at $10^{34}\,\mathrm{cm}^{-2}\mathrm{s}^{-1}$. The single particle track parameter resolutions and reconstruction efficiencies have been parametrised for use in the fast simulation, ATLFAST.

The TR performance of the TRT for π/e separation has been re-evaluated in the light of test-beam data. Compared to the performance reported in the ID TDR, the pion rejection has improved in the barrel by a factor of ~2, but has degraded in the end-cap by a factor of approximately 4 which depends critically on pseudorapidity. For a 90% electron efficiency, the pion rejection is typically around 40. A new result is that the TRT may be able to provide a statistical separation between pions and kaons of $>0.5\sigma$ up to a momentum of ~30 GeV – this is still being studied.

Algorithms have been developed which allow the primary vertices of hard-scattering collisions to be reconstructed at high luminosity. For $H \rightarrow \gamma\gamma$ (a difficult case since there are no primary tracks associated with the Higgs boson decay), an efficiency of ~70% can be achieved with a

background of around four vertices from pile-up events. In decays $B_d^0 \rightarrow J/\psi\, K_s^0$, the K_s^0 decays can be reconstructed with an efficiency of ~40%. The vertex *b*-tagging, discussed in Chapter 10, has improved significantly since the time of the ID TDR.

The alignment and calibration of the ID has been considered in more detail than before. To make a useful precision measurement of the *W* mass will require an understanding of the systematics on the momentum scale of better than 0.02%. This will be very challenging, but looks as if it may be possible.

To summarise: the Inner Detector will have a direct role in the physics of ATLAS, for example in *B* physics. In combination with the calorimeters, it will prove essential in identifying crucial physics signatures such as electrons and *b*-jets. Lastly, it will be valuable in calibrating other parts of ATLAS, in particular the EM Calorimeter.

3.9 References

3-1 ATLAS Collaboration, Inner Detector Technical Design Report Vol. I, CERN / LHCC 97-16 (1997).

3-2 ATLAS Collaboration, Inner Detector Technical Design Report Vol. II, CERN / LHCC 97-17 (1997).

3-3 ATLAS Collaboration, Pixel Technical Design Report, CERN / LHCC 98-13 (1998).

3-4 P. Luthaus, Ph.D. Thesis, University of Dortmund (1998)

3-5 A. Parker *et al.*, 'The Material Budget of the ATLAS Inner Detector', ATLAS Internal Note INDET-NO-207 (1998).

3-6 D. Barberis *et al.*, 'A Comparative Study of Reduced Layouts of the ATLAS Inner Detector', ATLAS Internal Note INDET-NO-188 (1997).

3-7 ATLAS Collaboration, Technical Coordination Technical Design Report, CERN / LHCC 99-01.

3-8 ATLAS Collaboration, Central Solenoid Technical Design Report, CERN / LHCC 97-21.

3-9 S. Sivoklokov, 'TRT Trigger Performance in the Solenoidal Magnetic Field', ATLAS Internal Note ATL-DAQ-004, INDET-99-005 (1999).

3-10 S. Haywood, 'Impact Parameter Resolution in the Presence of Multiple Scattering', ATLAS Internal Note INDET-NO-91 (1995).

3-11 E. Buis *et al.*, 'Parametrisation of the Inner Detector Performance', ATLAS Internal Note INDET-NO-197 (1997).

3-12 E. Buis *et al.*, 'Update of the Inner Detector Performance Parametrisations', ATLAS Internal Note INDET-NO-215 (1998).

3-13 N. Labanca, Ph.D. Thesis, University of Milano (1998).

3-14 U. Egede, Ph.D. Thesis, Lund University LUNFD6 / (NFFL-7150) (1997).

3-15 D. Rousseau, 'Hadron Identification in the TRT', ATLAS Internal Note ATL-COM-INDET-99-002 (1999).

3-16 L. Drage and A. Parker, 'An Investigation into the Effects of Increased SCT Noise and Inefficiency', ATLAS Internal Note, INDET-NO-181.

3-17 See for example: CDF Collaboration, Phys. Rev. **D52** (1995) 4784.

3-18 D. Froidevaux and M. Parker, 'The Performance Specifications of the ATLAS Inner Detector', ATLAS Internal Note, INDET-NO-046 (1994).

3-19 S. Haywood, 'Offline Alignment and Calibration of the Inner Detector', ATLAS Internal Note ATL-COM-INDET-99-001 (1999).

3-20 A. Bonissent *et al.*, 'Alignment of the Upgraded VDET at LEP2', ALEPH Internal Note ALEPH-97-116 (1997).

3-21 K. Abe *et al.*, Nucl. Instrum. Methods **A40** (1997) 287.

3-22 S. Peeters, 'Alignment of the ATLAS Precision Tracker using Tracks', ATLAS Internal Note ATL-COM-INDET-99-007 (1999).